Composites Part B 113 (2017) 225–242

Contents lists available at ScienceDirect

Composites Part B

journal homepage: www.elsevier.com/locate/compositesb

A continuum theory of through–the–thickness jacketed shells for the elasto-plastic analysis of confined composite structures: Theory and numerical assessment

S. Sessa [a], R. Serpieri [a, *], L. Rosati [b]

[a] Department of Engineering, University of Sannio, Piazza Roma, 21, 82100, Benevento, Italy
[b] Department of Structures for Engineering and Architecture, University of Naples Federico II, Via Claudio, 21, 80124, Napoli, Italy

ARTICLE INFO

Article history:
Received 15 October 2016
Received in revised form
4 January 2017
Accepted 8 January 2017
Available online 23 January 2017

Keywords:
Jacketed shell
Reinforced concrete
Masonry
Non linear analysis
Confinement

ABSTRACT

The paper proposes a generalized shell formulation devised for the triaxial stress analysis of Through-the-Thickness (TT) confining mechanisms induced by TT Jacketing (TTJ) devices in laminated composite structures, such as masonry walls retrofitted by stirrups-tied FRP sheets and TT jacketed concrete sandwich panels.

Assuming a smeared description of TT reinforcements, the proposed shell formulation is constructed as an enhancement of the classical laminated shell formulation based on the Equivalent Single Layer Mindlin First-order Shear Deformation Theory (ESL-FSDT). This enhancement captures TT stretching by adding the TT displacement field among the kinematic variables and permits to describe the smeared TTJ interaction between transverse uniaxial reinforcements and confined layers in terms of continuum equilibrium and compatibility equations. Statics and kinematics of the shell are developed by following standard work-association arguments and encompassing both TT-laminated and TT-functionally graded structures.

A nonlinear elasto-plastic constitutive behavior of the core material and of the TT reinforcements is considered and explicit representations of the elasto-plastic tangent operator are derived. The TTJ formulation is combined with a MITC finite element formulation and implemented in the research FE code Opensees.

Results of nonlinear structural analyses of walls subject to in-plane and out-of-plane bending show that the proposed TTJ approach provides physically meaningful predictions of the structural response and is capable to efficiently track a complex triaxial confining interaction which ultimately results into marked global structural effects of increased stiffness, strength and ductility.

© 2017 Elsevier Ltd. All rights reserved.

1. Introduction

The employment of confinement techniques for improving strength and ductility of structural members has progressively grown in popularity in parallel with the use of analytical and computational tools capable of describing their mechanics.

Confinement devices find typical applications in the reinforcement of existing concrete and masonry structures by steel bars, plates or Fiber Reinforced Polymers (FRP) [1–4], to increase the bearing capacity of both 1D members, such as columns and frames, or 2D members, such as shear walls, panels, slabs and curved shells.

Interest in the effect of through-the-thickness confinement in 2D elements has recently grown, in particular driven by innovative structural solutions. These concern several applications such as concrete sandwich panels [5] and masonry [6] in civil engineering, or more advanced ones in mechanical [7] and biomedical [8] engineering.

As well known, the desired gain in strength and ductility is an effect originated by the triaxiality, or biaxiality, of the stress state induced in the confined core material [9]. In line of principle, this effect can be enforced on members of any structural typology and depends on both the global geometry of the structure as well as on local details of the confinement device. However, for structural applications in civil engineering, the experimental characterization of confinement is mostly carried out over columns [10,11], and its

* Corresponding author.
E-mail address: rserpier@unisannio.it (R. Serpieri).

http://dx.doi.org/10.1016/j.compositesb.2017.01.011
1359-8368/© 2017 Elsevier Ltd. All rights reserved.

effect in the structural analysis of reinforced members is prevailingly taken into account in a simplified form, separating global and local mechanical analyses.

Relying on this separation, confinement devices are not ordinarily included as components of the global analysis; rather, the approach typically employed is the following: a local experimental and/or theoretical analysis of a confining device is preliminarily carried out to obtain suitably defined constitutive parameters which are subsequently employed in the global structural analyses in uncoupled form [1,10,12,13]. For 1D elements, this simplified approach is generally considered to be sufficiently accurate, as shown by several experimental investigations [1,14,15], providing also a basis for building code prescriptions [16–18].

Nevertheless, the analysis of confinement in 2D structural members is more complex since these elements can take advantage of both in-plane and transverse Through-the-Thickness (TT) confinement. The former is essentially a global structural effect, primarily dependent on the boundary conditions and ordinarily addressed by using membrane or shell Finite Elements Analysis (FEA) [19] in conjunction with suitable biaxial strength criteria [20,21]; conversely, the latter is accounted for at constitutive level though it is not always consistently incorporated in the global analysis.

In real applications of TT confinement over concrete and masonry walls transverse confinement is induced by reinforcing rods passing through the shell core; they tie the opposite exterior confining layers and the tying elements are uniformly distributed over large regions of the shell surface in regular arrays.

In particular, in RC walls, these ties correspond to transverse stirrups, forming the ordinary transverse steel reinforcement, whose confining effect has been experimentally highlighted in several studies [22–24], and whose design is also regulated by building codes [18,25]. For masonry, TT confinement has proved to be a convenient retrofit strategy by several experimental campaigns, in particular for stone walls [6] and multi–leafs ones [26] by using both FRP ties [27] and steel ties [28].

Investigations have also highlighted differences between the effect of Through-the-Thickness Jacketing (TTJ) observed in shear walls and in columns [29], since the strength increment due to confinement is critically influenced by the geometry of the reinforced structural member [30]. These experimental evidences show the meaningfulness of devising analysis methods for 2D shells/members removing the simplified assumption of a *tout-court* uncoupling between local and global responses.

Modeling of TT confinement requires a proper account of the presence of triaxial stress states inside the core material, on one side, and of differential TT elongations between the stirrups/ties and the confined core material, on the other one. Typically, in FEM analyses, both in–plane and through-the-thickness confinement are addressed by using 3D brick elements (core material) interacting with confining devices modeled as trusses, rods or external constraints (see, e.g., [31–33]). Regrettably, such a highly detailed 3D description requires significant computational efforts and can be hardly extended to global analyses of real structures in ordinary structural design.

On the other hand, it can be easily recognized that capturing of TT confinement, even in simplified form, in the context of a less computationally expensive 2D structural theory, is not trivial and cannot be achieved by ordinary theories of plates and shells. In particular, in order to have full development of TT confinement, differential displacements must be allowed at the core-tie interface. Moreover, a multilayered descriptions is required to account for the coexistence of exterior confining layers and interior confined core with different mechanical properties and stress states.

However, to the best of the authors' knowledge there exists no structural 2D continuum layered formulation suitable for describing the interaction of TT by-passing ties and confining/confined layers. This conclusion is gained after scoping the multiplicity of 2D formulations of layered plates and shells available to date, including Equivalent Single Layer (ESL) theories [34], the class of kinematically enriched shell formulations accounting for non-plane stress regimes [35,36] and/or addressing through-the-thickness stretching, or in the shell finite element proposed in Ref. [37], which introduces a transversal elongation degree of freedom (see, e.g., [38–40]).

A suitable formulation capable of describing TT confinement in simplified form seems to be not available even among nontraditional theories of plates and shells [41] or within the larger family of kinematically richer 2D shell theories, gathered under different denominations such as *layer-wise theories*, *discrete-layer theories* [34], *zig-zag theories* [42,43]. In particular these theories enforce interlaminar stress continuity by making the number of displacement variables dependent upon the number of constitutive layers of the shell.

Actually, while all the above mentioned formulations are well suited to address the presence of in–plane reinforcements [44–47], the TT interaction between ties and core material introduces an infringement of deformation continuity, as differential strains are typically present at the ties-core interface, and does not admit a simple layer-wise description since ties are punctual devices implying, on principle, a point-wise description.

In addition, it should also be observed that the mechanics of confinement–bearing devices becomes even more complex in the nonlinear range when, e.g., steel stirrups may yield or a crushing core may implode, as well as in presence of pre–stress.

On the basis of the previous considerations, aim of the present paper is the development of a suitable 2D continuum structural formulation for capturing the effects of TT confinement in nonlinear elasto-plastic structural analyses of layered shells.

A continuum theory with the above mentioned features is herein formulated proceeding from the adoption of a simplest possible enhancement of the classical laminated shell formulation based on ESL Mindlin First-order Shear Deformation Theory (ESL-FSDT). Such a theory is devised in order to capture the onset of triaxial stress states in the core material and to provide in a smeared form the description of the TTJ interaction, between transverse uniaxial reinforcement and confined layers, in terms of continuum equations of equilibrium and compatibility.

More specifically, the detailed objectives of the present work are to:

i) present the generalized kinematics and statics of the enhanced TTJ formulation following standard work-association arguments, within a more general description which accounts for the presence of a smeared distribution of TT reinforcement encompassing both TT-laminated and TT-functionally graded structures;
ii) derive a TT-continuum theory, with the related system of compatibility and equilibrium equations, from the more general continuum framework, and the related continuum tangent operator to be employed in return mapping schemes for the analysis of the confining interaction adopting elasto-plastic laws for the ties and the confined materials;
iii) combine this theoretical/numerical framework with established finite element formulations in order to carry out nonlinear structural analyses assessing the predicted global response for plane shells.

With specific reference to point 1), structural simulations herein reported have been carried out by implementing the laminated TTJ

schemes in the framework of a MITC shell element formulation [48,49]. This element has been purposefully chosen since it behaves well in the thin shell limit, avoiding locking phenomena, and has been used also in elasto-plastic analyses [50] as well as in presence of lamination [51]; moreover, it is available in the open-source research FEM code OpenSees [52].

The paper is organized as follows. In Section 2 the TTJ shell formulation is presented in the form of a more general theory encompassing both laminated and functionally graded structures. Numerical applications assessing the response of the TT confined shell formulation and the behavior of the employed numerical methods are presented in Section 3. Concluding remarks are finally reported in Section 4.

2. Smeared TTJ formulation

This section details the smeared shell formulation for Through-the-Thickness Jacketing (TTJ). Proceeding from the introduction of general assumptions on the continuum description of the shell configuration, on its kinematics and on the elasto-plastic constitutive assumptions, the work-associated stress measures of the TTJ shell model are first derived. They are subsequently employed in the formulation of the equations of equilibrium and compatibility representing the Through-the-Thickness (TT) confinement. The section is concluded with the derivation of the continuum elasto-plastic tangent operators which consistently linearize the nonlinear equations of the TTJ shell model.

A shell theory is considered so that we make reference to the median plane $\mathscr{S}$ of the shell. This is shown in Fig. 1 together with a Cartesian reference frame x, y and z, z being the coordinate directed along the thickness, and x, y the in-plane coordinates. The associated unit vectors are denoted by $\widehat{\mathbf{x}}$, $\widehat{\mathbf{y}}$ and $\widehat{\mathbf{z}}$. For simplicity, the shell thickness δ is assumed constant and the origin of the reference frame is located at the shell midplane, which is plotted in green, so that the exterior layers have coordinates $z = -\delta/2$ and $z = \delta/2$.

In the present study attention is focused on infinitesimal kinematics so that the deformed geometry of the shell is defined, at the continuum 3D level, by the infinitesimal displacement field $\mathbf{u}(x, y, z)$.

With a view towards implementation in FEM codes, a suitable matrix notation is employed throughout this section for stress, strain and stiffness quantities alongside with ordinary tensorial notation. The adopted matrix notation is set as a variant of Voigt's notation in which the entries associated with TT strain/stretch coordinates are moved to the rightmost position in row vectors.

The arrays constructed on the basis of this convention are denoted by a $(\cdot)_V$ subscript. This convention implies that the column vectors employed for representing strain and stress tensors are:

$$\boldsymbol{\varepsilon}_V = \begin{bmatrix} \varepsilon_x & \varepsilon_y & \gamma_{xy} & \gamma_{xz} & \gamma_{yz} & \varepsilon_z \end{bmatrix}^T \tag{1}$$

and

$$\boldsymbol{\sigma}_V = \begin{bmatrix} \sigma_x & \sigma_y & \tau_{xy} & \tau_{xz} & \tau_{yz} & \sigma_z \end{bmatrix}^T. \tag{2}$$

Furthermore, collecting the first five components of $\boldsymbol{\varepsilon}_V$ into the 1×5 vector $\boldsymbol{\varepsilon}_{0V}$ the following split is considered

$$\boldsymbol{\varepsilon}_V = \begin{bmatrix} \boldsymbol{\varepsilon}_{0V} \\ \varepsilon_z \end{bmatrix} = \begin{bmatrix} \overbrace{\varepsilon_x \quad \varepsilon_y \quad \gamma_{xy} \quad \gamma_{xz} \quad \gamma_{yz}}^{\boldsymbol{\varepsilon}_{0V}} & \varepsilon_z \end{bmatrix}^T \tag{3}$$

and a similar partition is considered also for the stress vector in (2)

$$\boldsymbol{\sigma}_V = \begin{bmatrix} \boldsymbol{\sigma}_{0V} \\ \sigma_z \end{bmatrix} = \begin{bmatrix} \overbrace{\sigma_x \quad \sigma_y \quad \tau_{xy} \quad \tau_{xz} \quad \tau_{yz}}^{\boldsymbol{\sigma}_{0V}} & \sigma_z \end{bmatrix}^T. \tag{4}$$

Application of these conventions to fourth-order symmetric tensor operators permits to represent them by matrices which are partitioned in four submatrices in the form exemplified below for the elastic stiffness tensor $\mathbb{C}$

$$\mathbb{C}_V = \begin{bmatrix} \mathbb{C}^{0\,0}{}_V & \mathbf{C}^{0\,z}{}_V \\ \mathbf{C}^{z\,0}{}_V & C^{z\,z}{}_V \end{bmatrix}, \tag{5}$$

where $\overset{z\,z}{C}{}_V = C_{zzzz}$ and

$$\mathbb{C}^{0\,0}{}_V = \begin{bmatrix} C_{xxxx} & C_{xxyy} & C_{xxxy} & C_{xxxz} & C_{xxyz} \\ C_{yyxx} & C_{yyyy} & C_{yyxy} & C_{yyxz} & C_{yyyz} \\ C_{xyxx} & C_{xyyy} & C_{xyxy} & C_{xyxz} & C_{xyyz} \\ C_{xzxx} & C_{xzyy} & C_{xzxy} & C_{xzxz} & C_{xzyz} \\ C_{yzxx} & C_{yzyy} & C_{yzxy} & C_{yzxz} & C_{yzyz} \end{bmatrix}, \tag{6}$$

$$\mathbf{C}^{z\,0}{}_V = \begin{bmatrix} C_{zzxx} & C_{zzyy} & C_{zzxy} & C_{zzxz} & C_{zzyz} \end{bmatrix}, \tag{7}$$

$$\mathbf{C}^{0\,z}{}_V = \begin{bmatrix} C_{xxzz} & C_{yyzz} & C_{xyzz} & C_{xzzz} & C_{yzzz} \end{bmatrix}^t. \tag{8}$$

As a shorthand notation, Gibbs Nabla operator ∇ is used to denote 3D gradients of vector fields while ∇_p is the gradient operator with respect to in plane variables x and y.

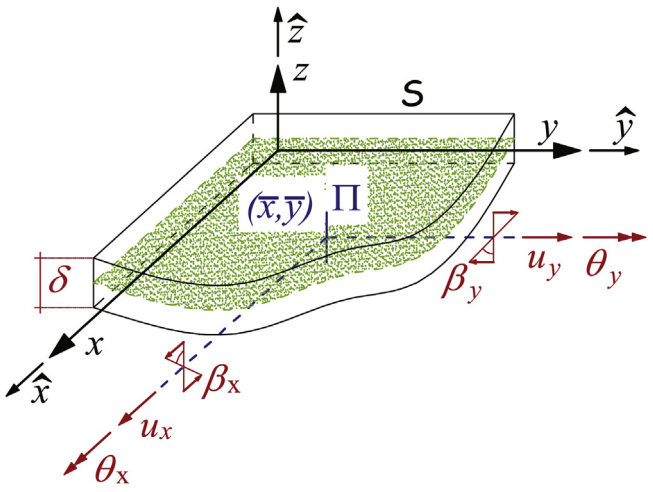

Fig. 1. Shell geometry and generalized displacement components.

2.1. General configuration assumptions

The formulation of the TTJ shell is herein devised as an enhancement of the Equivalent Single Layer First-order Shear Deformation Theory (ESL-FSDT) [34] by accounting for the presence of a smeared TT reinforcement.

This is described by a continuum scalar field μ_t, denominated *TT-reinforcement area ratio*, smearing the TT reinforcement onto the shell midplane. The field μ_t, defined over the shell midplane, associates with the generic midplane point $(\bar{x}, \bar{y})$ the relevant ratio of the cross-sectional area Ω_t of (discrete) TT by-passing ties per unit core shell midplane area Ω_c:

$$\mu_t = \frac{\Omega_t}{\Omega_c}. \tag{9}$$

By *shell chord*, $\Pi(\bar{x},\bar{y})$, located at the surface point $(\bar{x},\bar{y})$ we refer to the mechanical subsystem constituted by the material points of the shell which have coordinates $(x=\bar{x}, y=\bar{y}, z\in[-\delta/2,\delta/2])$ and to its relevant mechanical properties.

In each shell chord a tripartition is considered into a *core region* Π_c, which directly interacts with the TT reinforcement and which is potentially subject to a full triaxial stress state, plus two exterior *unconfined regions* undergoing plane stress conditions, Π_u^- and Π_u^+. Henceforth, for simplicity these regions are considered to have uniform thickness, and denominated *core layer* and *unconfined layers*. Accordingly, upon specifying the pair of (constant) coordinates z_c^- and z_c^+ such that $-\delta/2 < z_c^- < z_c^+ < \delta/2$, the range of Π_c is defined by the set $z\in[z_c^-, z_c^+]$ while the unconfined regions Π_u^-, Π_u^+ correspond to the sets $z\in[-\delta/2, z_c^-]$ and $z\in[z_c^+, \delta/2]$, respectively.

The above introduced tripartition is exemplified in Fig. 2 with reference to the plastic (steel) reinforcements typically employed in masonry (concrete) walls. In this case the coefficient μ_t corresponds to the transverse area (per square unit reference area) of stirrups crossing the middle plane of the wall; in these examples the core layer can be straightforwardly identified with the masonry (concrete) material contained in between the in-plane sheets of FRP (steel) reinforcements tied with stirrups.

2.2. TT heterogeneity and constitutive assumptions

Heterogeneity of constitutive properties across the thickness is assumed. For layers and TT reinforcements, attention is hereby confined to an associative elasto-plastic constitutive behavior [53,54].

The assumptions above and the employed linearized kinematic framework imply that the internal state of the generic point **x** located at a generic quota z belonging to the shell chord $\Pi(\bar{x},\bar{y})$ is defined by the three-dimensional (total) strain tensor,

$$\boldsymbol{\varepsilon} = \mathrm{sym}(\mathbf{u}\otimes\nabla) \tag{10}$$

plus the tensor of plastic strain $\boldsymbol{\varepsilon}^p$. The stress-strain relation is given by the plastic strain tensor:

$$\boldsymbol{\sigma} = \mathbb{C}(\boldsymbol{\varepsilon} - \boldsymbol{\varepsilon}^p) \tag{11}$$

where $\mathbb{C}$ is the elastic fourth-order tensor with components C_{ijhk}. For generality, anisotropy is considered; this corresponds to the existence of 21 independent coefficients C_{ijhk} fulfilling major, $C_{ijhk} = C_{hkij}$, and minor symmetries, $C_{ijhk} = C_{jihk} = C_{ijkh}$.

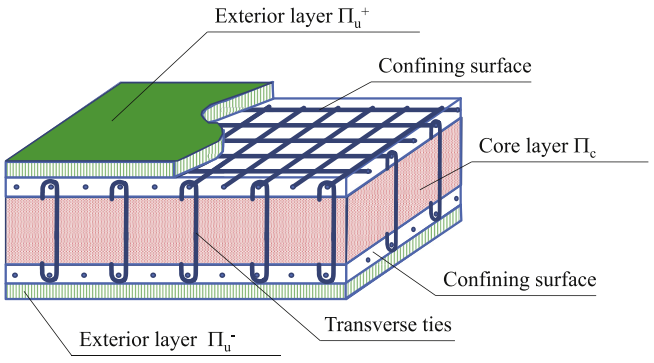

Fig. 2. Sketch of a typical RC wall partition into core layer/exterior layers.

The evolution law of $\boldsymbol{\varepsilon}^p$ is defined in rate terms with the aid of a plastic multiplier λ evolving as dictated by Karush-Kuhn-Tucker conditions [55,56]:

$$\dot{\boldsymbol{\varepsilon}}^p = \dot{\lambda}\frac{\partial f}{\partial \boldsymbol{\sigma}}, \qquad \dot{\lambda} \geq 0, \quad f(\boldsymbol{\sigma}) \leq 0, \quad \dot{\lambda} f = 0, \tag{12}$$

where f is a convex yield function.

To encompass a sufficiently comprehensive family of elasto-plastic behaviors, associated with a generic point **x**, dependence of f upon all three stress invariants is considered, viz.:

$$f = aJ_2 + bI_1 + cJ_3 + d, \tag{13}$$

where I_1 is the first invariant of the stress tensor, J_2 and J_3 are the second and third invariants of the deviatoric part, $\mathrm{dev}\boldsymbol{\sigma}$, of the stress tensor:

$$I_1 = \mathrm{tr}\boldsymbol{\sigma}, J_2 = (\mathrm{dev}\boldsymbol{\sigma}\cdot\mathrm{dev}\boldsymbol{\sigma})^{1/2}, J_3 = \det(\mathrm{dev}\boldsymbol{\sigma}), \tag{14}$$

while a, b, c and d are scalar coefficients fulfilling the convexity of f.

In particular yield functions associated with Von Mises and Drucker-Prager criteria are retrieved as special cases of (13). Specifically, denoting by σ_0 the uniaxial yield stress, Equation (13) specializes to the Von Mises yield criterion with $a=\sqrt{3}$, $b=c=0$, $d=-\sigma_0$. Moreover, denoting by σ_t and σ_c the tensile and compressive yield stresses and setting

$$a = 1; \quad b = -\frac{1}{\sqrt{3}}\left(\frac{\sigma_t - \sigma_c}{\sigma_t + \sigma_c}\right), \qquad c = 0; \quad d = -\frac{2}{\sqrt{3}}\left(\frac{\sigma_t\sigma_c}{\sigma_t + \sigma_c}\right), \tag{15}$$

the Drucker Prager criterion is desumed from (13).

Through-the thickness heterogeneity is accounted for by assuming that, for a given shell chord $\Pi(\bar{x},\bar{y})$, coefficients a, b, c, d as well as coefficients C_{ijhk} are function of z. To encompass a more general through-the-thickness distribution of mechanical properties, namely both TT-laminated and TT-functionally graded structures, functions $a(z)$, $b(z)$, $c(z)$, $d(z)$ and $C_{ijhk}(z)$ are assumed to be a combination of piecewise constant functions (laminated structure) and piecewise linear functions (functionally graded structure).

Relationships between work-associated generalized stress variables and generalized strain variables are represented with the aid of an Helmoltz free energy functional $\Phi(\boldsymbol{\alpha}_i, \boldsymbol{\alpha}_j, \boldsymbol{\alpha}_k)$ of three generic (scalar, vector or tensor) mechanical descriptors $\boldsymbol{\alpha}_i$, $\boldsymbol{\alpha}_j$ and $\boldsymbol{\alpha}_k$, (which can be scalar variables or functions); the usual notation $\partial\Phi/\partial\boldsymbol{\alpha}_i$ denotes the standard partial differentiation carried out by varying $\boldsymbol{\alpha}_i$ while holding fixed all remaining state descriptors.

As a standard application of the work-association concept, upon introducing the free energy function $\Phi(\boldsymbol{\varepsilon}, \boldsymbol{\varepsilon}^p)$, the mechanical quantities entering (11) can be framed within the continuum thermomechanics with internal variables [57–59] where the stress tensor $\boldsymbol{\sigma}$ is the mechanical quantity work-associated with the total strain $\boldsymbol{\varepsilon}$, [53,54], viz.:

$$\boldsymbol{\sigma} = \frac{\partial\Phi}{\partial\boldsymbol{\varepsilon}} = \frac{\partial\Phi}{\partial\boldsymbol{\varepsilon}}\bigg|_{\overbrace{\boldsymbol{\varepsilon}^p}^{fix.}}. \tag{16}$$

In (16) the subscript $\boldsymbol{\varepsilon}^p$ under the $\overbrace{(\cdot)}^{fix.}$ sign is used to remark that this quantity is held fixed. Using the same notation to represent

fourth-order stiffness operators, the elastic stiffness operator is defined as:

$$\mathbb{C} = \frac{\partial \boldsymbol{\sigma}}{\partial \boldsymbol{\varepsilon}} = \frac{\partial \boldsymbol{\sigma}}{\partial \boldsymbol{\varepsilon}}\bigg|_{\underbrace{\boldsymbol{\varepsilon}^p}_{fix.}} = \frac{\partial^2 \Phi}{\partial \boldsymbol{\varepsilon} \otimes \partial \boldsymbol{\varepsilon}}\bigg|_{\underbrace{\boldsymbol{\varepsilon}^p}_{fix.}}. \tag{17}$$

The notation in (16) is also conveniently employed in Subsection 2.4 to represent in a short-hand format the work-association relationships between generalized stress variables and generalized strain variables entering the TTJ shell formulation.

A different derivative concept is the differentiation of a free energy functional Φ, with respect to a descriptor $\boldsymbol{\alpha}_i$, carried out while the mechanical system remains *relaxed* over some descriptors $\boldsymbol{\alpha}_j$ and $\boldsymbol{\alpha}_k$, i.e., letting $\boldsymbol{\alpha}_j$, $\boldsymbol{\alpha}_k$ evolve in fulfillment of underlying evolution laws dictated by lower-scale equilibrium, or by thermodynamic laws. This differentiation operation, which is herein denoted as:

$$\frac{\partial \Phi}{\partial \boldsymbol{\alpha}_i}\bigg|_{\underbrace{\boldsymbol{\alpha}_j, \boldsymbol{\alpha}_k}_{rel.}}, \tag{18}$$

permits to conveniently represent the elasto-plastic tangent operator $\mathbb{C}^{ep}$ of the material constituting the shell at a point $\mathbf{x}$. It enters the explicit rate form of the stress-strain relation

$$\dot{\boldsymbol{\sigma}} = \mathbb{C}^{ep}\dot{\boldsymbol{\varepsilon}}, \tag{19}$$

or in the compact form

$$\mathbb{C}^{ep} = \frac{\partial \boldsymbol{\sigma}}{\partial \boldsymbol{\varepsilon}}\bigg|_{\underbrace{\boldsymbol{\varepsilon}^p}_{rel.}}. \tag{20}$$

As well known [53], the expression of $\mathbb{C}^{ep}$ for the rate-independent work-associated perfect plasticity herein considered is:

$$\mathbb{C}^{ep} = \begin{cases} \mathbb{C} & \dot{\lambda} = 0 \\ \mathbb{C} - \left(\frac{\partial f}{\partial \boldsymbol{\sigma}} \cdot \mathbb{C} \frac{\partial f}{\partial \boldsymbol{\sigma}}\right)^{-1} \mathbb{C}\left(\frac{\partial f}{\partial \boldsymbol{\sigma}} \otimes \frac{\partial f}{\partial \boldsymbol{\sigma}}\right)\mathbb{C} & \dot{\lambda} > 0 \end{cases}. \tag{21}$$

Fourth order tensors $\mathbb{C}$, $\mathbb{C}^{ep}$ are also represented in the Voigt-similar matrix notation reported in (5)–(8), respectively as $\mathbb{C}_V$ and $\mathbb{C}_V^{ep}$. This permits to represent relation (19) in the Voigt form:

$$\dot{\boldsymbol{\sigma}}_V = \mathbb{C}_V^{ep}\dot{\boldsymbol{\varepsilon}}_V. \tag{22}$$

An elasto-plastic stress-strain response is considered also for the constitutive response of the transversal ties. The relevant laws can be straightforwardly obtained by specializing to the uniaxial case their triaxial counterparts recalled above. Specifically, denoting by σ_t, ε_t and ε_t^p, respectively, the scalar stress, elastic and plastic strains of the ties (smeared onto the median plane), and by Φ_t the smeared free energy of the ties, one has:

$$\sigma_t = C_t\left(\varepsilon_t - \varepsilon_t^p\right), \quad \sigma_t = \frac{\partial \Phi_t}{\partial \varepsilon_t}\bigg|_{\underbrace{\varepsilon_t^p}_{fix.}}. \tag{23}$$

The corresponding rate incremental stress-strain law is:

$$\dot{\sigma}_t = C_t^{ep}\dot{\varepsilon}_t, \tag{24}$$

where C_t^{ep} is the (smeared) tangent elasto-plastic operator associated with the (nonlinear) constitutive function of the transverse reinforcement material, an operator that can be operatively computed as a 1D specialization of (21).

2.3. Kinematics of the TTJ shell

The kinematics of the proposed TTJ formulation is devised as an enrichment of the generalized displacement fields of a standard ESL-FSDT formulation [34,60] by supplementing the generic shell chord $\Pi(\bar{x},\bar{y})$ with a TT transverse displacement field $u_z(z)$. This enrichment has the objective of describing stretches along-the-thickness, yet ensuring TT continuity of stresses σ_z on account of its key role in TT confinement.

We recall that, within the standard FSDT of planar shells, the generalized displacements $\mathscr{u}_V^{\Pi}(\bar{x},\bar{y})$ of chord $\Pi(\bar{x},\bar{y})$ are

$$\mathscr{u}_V^{\Pi}(\bar{x},\bar{y}) = \left[\mathbf{u}^{(m)}(\bar{x},\bar{y}) \quad \boldsymbol{\beta}(\bar{x},\bar{y})\right]^T \tag{25}$$

where $\mathbf{u}^{(m)}$ is the field of in-plane membrane displacements and $\boldsymbol{\beta}$ is the field of generalized plate displacements:

$$\mathbf{u}^{(m)} = \left[u_x^{(m)} \quad u_y^{(m)}\right]^T, \tag{26}$$

$$\boldsymbol{\beta} = \left[\beta_x \quad \beta_y\right]^T. \tag{27}$$

Fig. 1 provides graphical illustrations recalling the elementary 3D displacements of the shell associated with individual unit values of the coordinates appearing in (26) and (27); in particular, vector $\boldsymbol{\beta}$ is related to the rotations about axes x and y, $\boldsymbol{\theta} = \left[\theta_x \quad \theta_y\right]^T$, by means of $\boldsymbol{\beta} = \widehat{\mathbf{z}} \times \boldsymbol{\theta} = \left[-\theta_y \quad \theta_x\right]^T$. Rotations θ_x and θ_y are assumed positive if counter-clockwise.

The inclusion of the TT transverse displacement field $u_z(z)$ among the kinematic descriptors of the shell chord implies that the state of $\Pi(\bar{x},\bar{y})$ is defined by:

$$\Pi(\bar{x},\bar{y}) \rightarrow \quad \mathscr{u}_V^{\Pi}, u_z(z) \tag{28}$$

where $(\bar{x},\bar{y}) \in \mathscr{S}$ and $z \in [-\delta/2, \delta/2]$. Hence, the relation between generalized shell displacements and 3D displacements reads:

$$\mathbf{u} = \mathbf{u}^{(m)} + \boldsymbol{\theta} \times z\widehat{\mathbf{z}} + u_z(z)\widehat{\mathbf{z}}, \tag{29}$$

where dependence upon variables $\bar{x}$ and $\bar{y}$ has been omitted.

Strain components from ordinary ESL-FSDT are grouped below in the vector:

$$\boldsymbol{\varepsilon}_V^{\Pi} = \left[\mathscr{E}_x^m \quad \mathscr{E}_y^m \quad \gamma_{xy}^m \quad \kappa_x^b \quad \kappa_y^b \quad 2\kappa_{xy}^b \quad \gamma_{xz}^s \quad \gamma_{yz}^s\right]^T \tag{30}$$

whose entries are the components of membrane strain measures $\boldsymbol{\varepsilon}^m$, bending strains $\boldsymbol{\varepsilon}^b$ and shear strain measures $\boldsymbol{\varepsilon}^s$. Their relation with generalized FSDT displacements is recalled below

$$\boldsymbol{\varepsilon}^m = \mathrm{sym}\left(\mathbf{u}^{(m)} \otimes \nabla_p\right) = \begin{bmatrix} \mathscr{E}_x^m & \gamma_{xy}^m/2 \\ \gamma_{xy}^m/2 & \mathscr{E}_y^m \end{bmatrix} \tag{31}$$

$$\mathscr{E}^b = \mathrm{sym}\left(\widehat{\mathbf{z}} \times \boldsymbol{\theta} \otimes \nabla_p\right) = \mathrm{sym}(\boldsymbol{\beta} \otimes \nabla_p)$$
$$= \begin{bmatrix} \dfrac{\partial \beta_x}{\partial x} & \dfrac{1}{2}\left(\dfrac{\partial \beta_x}{\partial y} + \dfrac{\partial \beta_y}{\partial x}\right) \\ \dfrac{1}{2}\left(\dfrac{\partial \beta_x}{\partial y} + \dfrac{\partial \beta_y}{\partial x}\right) & \dfrac{\partial \beta_y}{\partial y} \end{bmatrix} = \begin{bmatrix} \kappa_x^b & \dfrac{\kappa_{xy}^b}{2} \\ \dfrac{\kappa_{xy}^b}{2} & -\kappa_y^b \end{bmatrix} \tag{32}$$

The whole set of chord strains includes the shear strains γ_{xz} and γ_{yz}

$$\boldsymbol{\varepsilon}^s = \begin{bmatrix} \frac{\partial u_z}{\partial x} + \beta_x & \frac{\partial u_z}{\partial y} - \beta_y \end{bmatrix}^T = \begin{bmatrix} \gamma_{xz} & \gamma_{yz} \end{bmatrix}^T. \tag{33}$$

As a result of the adoption of descriptors in (28), the set of enriched strain measures of the shell chord is

$$\Pi(\overline{x}, \overline{y}) \rightarrow \quad \mathscr{E}_V^{\Pi}, \varepsilon_z(z), \tag{34}$$

where $\varepsilon_z = \partial u_z / \partial z$.

The tensor relation between 3D continuum strains and generalized TTJ strains is accordingly:

$$\boldsymbol{\varepsilon} = \widehat{\mathscr{E}}^m - z\widehat{\mathscr{E}}^b + \gamma_{xz}\frac{1}{2}\left(\widehat{\mathbf{x}} \otimes \widehat{\mathbf{z}} + \widehat{\mathbf{z}} \otimes \widehat{\mathbf{x}}\right) + \gamma_{yz}\frac{1}{2}\left(\widehat{\mathbf{y}} \otimes \widehat{\mathbf{z}} + \widehat{\mathbf{z}} \otimes \widehat{\mathbf{y}}\right) + \varepsilon_z\left(\widehat{\mathbf{z}} \otimes \widehat{\mathbf{z}}\right), \tag{35}$$

where the superposed hat over $\boldsymbol{\varepsilon}^m$ and $\boldsymbol{\varepsilon}^b$ denotes their immersion in the space of 3D second order symmetric tensors, what corresponds, for instance, to:

$$\widehat{\boldsymbol{\varepsilon}}^m = \begin{bmatrix} \mathscr{E}_x^m & \gamma_{xy}^m/2 & 0 \\ \gamma_{xy}^m/2 & \mathscr{E}_y^m & 0 \\ 0 & 0 & 0 \end{bmatrix}. \tag{36}$$

Relation (35) can be conveniently rewritten in Voigt-like matrix form. Using (30) and with the aid of the following matrix projectors:

$$\overset{0}{\mathbb{P}}_V(z) = \begin{bmatrix} 1 & 0 & 0 & -z & 0 & 0 & 0 & 0 \\ 0 & 1 & 0 & 0 & -z & 0 & 0 & 0 \\ 0 & 0 & 1 & 0 & 0 & -z & 0 & 0 \\ 0 & 0 & 0 & 0 & 0 & 0 & 1 & 0 \\ 0 & 0 & 0 & 0 & 0 & 0 & 0 & 1 \\ 0 & 0 & 0 & 0 & 0 & 0 & 0 & 0 \end{bmatrix} \tag{37}$$

and

$$\mathbf{P}^z{}_V = \begin{bmatrix} 0 & 0 & 0 & 0 & 0 & 1 \end{bmatrix}^T, \tag{38}$$

the following relation holds

$$\boldsymbol{\varepsilon}_V = \overset{0}{\mathbb{P}}_V(z)\boldsymbol{\varepsilon}_V^{\Pi} + \varepsilon_z(z)\overset{z}{\mathbf{P}}_V \tag{39}$$

from which one also deduces

$$\frac{\partial \boldsymbol{\varepsilon}_V}{\partial \boldsymbol{\varepsilon}_V^{\Pi}} = \overset{0}{\mathbb{P}}_V(z). \tag{40}$$

In order to simplify some matrix operations reported in the sequel, it is also convenient to consider the upper 5×8 submatrix of (37) (denoted by a starred superscript)

$$\overset{0}{\mathbb{P}}{}_V^{\star}(z) = \begin{bmatrix} 1 & 0 & 0 & -z & 0 & 0 & 0 & 0 \\ 0 & 1 & 0 & 0 & -z & 0 & 0 & 0 \\ 0 & 0 & 1 & 0 & 0 & -z & 0 & 0 \\ 0 & 0 & 0 & 0 & 0 & 0 & 1 & 0 \\ 0 & 0 & 0 & 0 & 0 & 0 & 0 & 1 \end{bmatrix} \tag{41}$$

whereby vector $\boldsymbol{\varepsilon}_{0V}$ can be represented as

$$\boldsymbol{\varepsilon}_{0V}(z) = \mathbb{P}_V^{\star}(z)\,\mathscr{E}_{V.}^{\Pi} \tag{42}$$

2.4. Stress measures of the TTJ shell

Generalized stress measures of the shell chord are also defined in terms of work-association in relation to the free energy Φ^{Π} of $\Pi(\overline{x}, \overline{y})$:

$$\Phi^{\Pi}(\overline{x}, \overline{y}) = \int_{-\delta/2}^{\delta/2} \Phi(\overline{x}, \overline{y}, z)\, dz. \tag{43}$$

Specifically, the eight-entries vector of generalized stress measures of the shell can be directly introduced in Voigt notation as follows:

$$\boldsymbol{\sigma}_V^{\Pi} = \frac{\partial \Phi^{\Pi}}{\partial \boldsymbol{\varepsilon}_V^{\Pi}}. \tag{44}$$

Owing to the addition of the degrees of freedom represented by field $u_z(z)$, describing TT stretch of the core chord and of the exterior unconfined layers, the stress state of a chord $\Pi(\overline{x}, \overline{y})$ is characterized by the following triplet of generalized stress measures

$$\boldsymbol{\sigma}_V^{\Pi}, \sigma_t, \sigma_z(z), \tag{45}$$

where $\boldsymbol{\sigma}_V^{\Pi}$ captures the FSDT deformation component of $\Pi(\overline{x}, \overline{y})$, σ_t the smeared stress in the ties (assumed constant in the core layer), and $\sigma_z(z)$ is such that $\sigma_z = 0$ for z belonging to the unconfined layers, i.e., for $z \in [-\delta/2, z_c^-]$ and $z \in [z_c^+, \delta/2]$.

The relation between 3D stress measures and generalized stress measures stems from work-association by application of the chain rule on account of (16), (40) and (43):

$$\boldsymbol{\sigma}_V^{\Pi} = \frac{\partial \Phi^{\Pi}}{\partial \mathscr{E}_V^{\Pi}} = \int_{-\delta/2}^{\delta/2} \frac{\partial \Phi^{\Pi}}{\partial \boldsymbol{\varepsilon}_V}(z)\frac{\partial \boldsymbol{\varepsilon}_V}{\partial \mathscr{E}_V^{\Pi}}(z)\, dz = \int_{-\delta/2}^{\delta/2} \left(\mathbb{P}_V\right)^T \boldsymbol{\sigma}_V\, dz. \tag{46}$$

It is worth being observed that, according to the previous relation, the generalized stress vector $\boldsymbol{\sigma}_V^{\Pi}$ does not depend on field $\sigma_z(z)$. This is a natural consequence of the fact that FSDT simply neglects TT stretching, while a complete description of the stress state in the present formulation is the one in (45).

The explicit relations between 3D stress components and generalized FSDT stress components are computed from (46). These

are reported below, grouped by membrane generalized stresses, plate generalized stresses and out-of-plane shear stresses:

$$\boldsymbol{\sigma}_V^m = \begin{bmatrix} \dfrac{\partial \Phi^\Pi}{\partial \mathscr{E}_x^m} \\ \dfrac{\partial \Phi^\Pi}{\partial \mathscr{E}_y^m} \\ \dfrac{\partial \Phi^\Pi}{\partial \gamma_{xy}^m} \end{bmatrix} = \begin{bmatrix} \int_{-\delta/2}^{\delta/2} \sigma_x \, dz \\ \int_{-\delta/2}^{\delta/2} \sigma_y \, dz \\ \int_{-\delta/2}^{\delta/2} \tau_{xy} \, dz \end{bmatrix} \tag{47}$$

$$\boldsymbol{\sigma}_V^b = \begin{bmatrix} \dfrac{\partial \Phi^\Pi}{\partial \kappa_x^b} \\ \dfrac{\partial \Phi^\Pi}{\partial \kappa_y^b} \\ \dfrac{1}{2}\dfrac{\partial \Phi^\Pi}{\partial \kappa_{xy}^b} \end{bmatrix} = \begin{bmatrix} \int_{-\delta/2}^{\delta/2} z\sigma_x \, dz \\ \int_{-\delta/2}^{\delta/2} z\sigma_y \, dz \\ \int_{-\delta/2}^{\delta/2} z\tau_{xy} \, dz \end{bmatrix} \tag{48}$$

$$\boldsymbol{\sigma}_V^s = \begin{bmatrix} \dfrac{\partial \Phi^\Pi}{\partial \gamma_{xz}^s} \\ \dfrac{\partial \Phi^\Pi}{\partial \gamma_{yz}^s} \end{bmatrix} = \begin{bmatrix} \int_{-\delta/2}^{\delta/2} \tau_{xz} \, dz \\ \int_{-\delta/2}^{\delta/2} \tau_{yz} \, dz \end{bmatrix} \tag{49}$$

$$\boldsymbol{\sigma}_V^\Pi = \frac{\partial \Phi^\Pi}{\partial \boldsymbol{\varepsilon}_V^\Pi} = \left[\boldsymbol{\sigma}_V^m \; \boldsymbol{\sigma}_V^b \; \boldsymbol{\sigma}_V^s \right]^T. \tag{50}$$

2.5. TTJ equilibrium and compatibility equations

The TTJ interaction between ties and core material is described based on the following assumptions:

- the opposite upper and lower ends of the ties are perfectly pointwise joined with the upper and lower boundary planes of the core layer, i.e., with planes $z = z_c^-$, $z = z_c^+$, respectively, so that the transverse displacements of the core and the stress of the ties are coincident at these locations: $u_z(z_c^-) = u_z^t(z_c^-)$, $u_z(z_c^+) = u_z^t(z_c^+)$;
- in the interior part of the core layer, $z_c^- < z < z_c^+$, tie-core interaction is absent, so that the core material and the ties can undergo completely independent deformations.

For a generic chord $\Pi(\bar{x}, \bar{y})$, the hypotheses above imply, on the one hand, the compatibility condition that the core elongation must be equal to the elongation of the ties, and, on the other hand, as a consequence of translational equilibrium along the z axis, the existence of a direct relation between the normal stresses along z of the shell core and of the ties, mediated by μ_t defined in (9). These conditions correspond to the following equations:

1 TTJS compatibility:

$$\int_{z_c^-}^{z_c^+} \varepsilon_z(z) \, dz = \varepsilon_t \delta_t \tag{51}$$

where $\delta_t = z_c^+ - z_c^-$.

2 TTJS equilibrium:

$$\Omega_c \sigma_z(z) + \Omega_t \sigma_t = 0, \quad \forall z \in \left] z_c^-, z_c^+ \right[. \tag{52}$$

The system composed by equations (51) and (52), combined with the constitutive equations of Section 2.2 and the kinematic equations of Section 2.3 (and with (9)), defines a continuous convex optimization problem, in the primary unknown field $u_z(z)$, describing the meso-scale response of the elasto-plastic TTJ shell chord $\Pi(\bar{x}, \bar{y})$ located at $(\bar{x}, \bar{y})$. This meso-scale problem is, in general, coupled with the global minimization problem expressing equilibrium of the shell at a structural level.

Hereby, it is convenient to consider the rate form of the local problem which is specially suited for handling elasto-plastic problems so as to derive an explicit relation for the elasto-plastic tangent operator of the shell chord, in a form analogous to the one provided by (20)–(22) for the standard 3D problem.

Following a conceptual scheme usual in strain-driven elasto-plasticity, the (rate-form) shell chord problem can be cast in a form such that the rate field $\dot{u}_z(z)$ is set as the primary unknown function, which all other unknown (rate) kinematic fields are related to, while $\dot{\boldsymbol{\varepsilon}}_V^\Pi$ is treated as the known driving vector variable.

Upon recalling definition (9) for μ_t and introducing the rate of TT elongation of the core layer $\dot{\delta}_t$ defined as:

$$\dot{\delta}_t = \int_{z_c^-}^{z_c^+} \dot{\varepsilon}_z(z) \, dz = \int_{z_c^-}^{z_c^+} \frac{\partial \dot{u}_z}{\partial z} \, dz = \dot{u}_z\left(z_c^+\right) - \dot{u}_z\left(z_c^-\right) \tag{53}$$

the rate forms of equations (51) and (52) are written as follows, respectively:

$$\dot{\delta}_t = \dot{\varepsilon}_t \delta_t \qquad \text{(compatibility in rate form)}, \tag{54}$$

$$\dot{\sigma}_z(z) + \mu_t \dot{\sigma}_t = 0 \qquad \text{(equilibrium in rate form)}, \tag{55}$$

where (55) holds for any $z \in]z_c^-, z_c^+[$.

To obtain the solution of the rate problem we combine (22) with the rate form of (39) and obtain

$$\dot{\boldsymbol{\sigma}}_V = \mathbb{C}_V^{ep}\left(\mathbb{P}_V(z) \, \dot{\mathscr{E}}_V^\Pi + \dot{\varepsilon}_z(z) \mathbf{P}^z{}_V \right) \tag{56}$$

Using (42) and recalling the Voigt-like matrix conventions (3)–(8) which separate the entries associated with the TT strain/stretch coordinates, the previous equation can be split in the following vector and scalar equations:

$$\dot{\boldsymbol{\sigma}}_{0V}(z) = \mathbb{C}_V^{ep} 0 \, 0(z) \mathbb{P}_V^\star(z) \, \dot{\mathscr{E}}_V^\Pi + \dot{\varepsilon}_z(z) \mathbf{C}_V^{ep} 0 \, z(z), \tag{57}$$

$$\dot{\sigma}_z(z) = \mathbf{C}_V^{ep} z \, 0(z) \cdot \mathbb{P}_V^\star(z) \, \dot{\mathscr{E}}_V^\Pi + C_V^{ep} z \, z(z) \dot{\varepsilon}_z(z). \tag{58}$$

The last equation can be inserted into (55), observing that $\dot{\varepsilon}_z = \partial \dot{u}_z / \partial z$ and that the relation $\dot{\sigma}_t = C_t^{ep} \dot{\delta}_t / \delta_t$ can be inferred from (24) and (54); this provides:

$$\frac{\partial \dot{u}_z}{\partial z}(z) - \mu_t \frac{C_t^{ep}}{C_V^{ep}{}_{z\,z}}(z)\,\dot{\delta}_t \Big/ \delta_t = -\frac{1}{C_V^{ep}{}_{z\,z}}(z)\mathbf{C}_V^{ep}{}_{z\,0}(z)\cdot\mathbb{P}_V^{\star}(z)\,\dot{\mathscr{E}}_V^{\Pi}. \tag{59}$$

Integration of the previous relation in the interval $]z_c^-, z_c^+[$ yields

$$\begin{aligned}&\int_{z_c^-}^{z_c^+} \frac{\partial \dot{u}_z}{\partial z}(z)\,dz - \mu_t \int_{z_c^-}^{z_c^+} \frac{C_t^{ep}}{C_V^{ep}{}_{z\,z}}(z)\dot{\delta}_t \Big/ \delta_t\,dz \\ &= -\int_{z_c^-}^{z_c^+} \frac{1}{C_V^{ep}{}_{z\,z}}(z)\mathbf{C}_V^{ep}{}_{z\,0}(z)\cdot\mathbb{P}_V^{\star}(z)\,\dot{\mathscr{E}}_V^{\Pi}\,dz,\end{aligned} \tag{60}$$

or, equivalently:

$$\dot{\delta}_t - \mu_t \frac{\dot{\delta}_t}{\delta_t} C_t^{ep} \int_{z_c^-}^{z_c^+} \frac{1}{C_V^{ep}{}_{z\,z}}(z)\,dz = -\left(\int_{z_c^-}^{z_c^+} \frac{1}{C_V^{ep}{}_{z\,z}}(z)\left(\mathbb{P}_V^{\star}(z)\right)^T \mathbf{C}_V^{ep}{}_{z\,0}(z)\,dz\right)\dot{\mathscr{E}}_V^{\Pi}. \tag{61}$$

Thus, setting

$$\mathscr{V} = -\frac{\left(\int_{z_c^-}^{z_c^+} \frac{1}{C_V^{ep}{}_{z\,z}(z)} \left(\mathbb{P}_V^{\star}{}_{\,0}^{\,z}(z)\right)^T \mathbf{C}_V^{ep}{}_{z\,0}(z)\,dz\right)}{1 - \frac{\mu_t}{\delta_t} C_t^{ep} \int_{z_c^-}^{z_c^+} \frac{1}{C_V^{ep}{}_{z\,z}(z)}\,dz} \tag{62}$$

$\dot{\delta}_t$ is finally computed as:

$$\dot{\delta}_t = \mathscr{V}\cdot\dot{\boldsymbol{\varepsilon}}_V^{\Pi} \tag{63}$$

When field $\dot{u}_z(z)$ evolves in compliance with (65) we say that the mechanical system Π_c of the core layer is *relaxed* with respect to field u_z, i.e., it evolves in fulfillment of equilibrium and elasto-plastic constitutive laws.

Employing the same notation as in (20) the elasto-plastic tangent operator $\mathbb{H}_V$ of the chord Π, entering its rate constitutive law

$$\dot{\boldsymbol{\sigma}}_V^{\Pi} = \mathbb{H}_V\ \dot{\mathscr{E}}_{V,}^{\Pi} \tag{66}$$

can be represented as

$$\mathbb{H}_V = \frac{\partial \boldsymbol{\sigma}_V^{\Pi}}{\partial \mathscr{E}_V^{\Pi}}\Big|_{\underbrace{u_z}_{rel.}}. \tag{67}$$

Hence, substituting (46) into (67) one computes

$$\mathbb{H}_V = \int_{-\delta/2}^{\delta/2} \left(\mathbb{P}_V^{\star}\right)^T \frac{\partial \boldsymbol{\sigma}_V}{\partial \mathscr{E}_V^{\Pi}}\Big|_{\underbrace{u_z}_{rel.}} dz, \tag{68}$$

where the term $\partial\boldsymbol{\sigma}_V/\partial\boldsymbol{\varepsilon}_V^{\Pi}|_{\underbrace{u_z}_{rel.}}$ is computed, for z belonging to the confined core chord Π_c and, accounting for the *relaxed* expression of $\dot{\varepsilon}_z$ provided by (64), from (57), (58). In particular, for the confined core chord Π_c substitution of Equation (64) into (57) yields

$$\dot{\boldsymbol{\sigma}}_{0V}(z) = \frac{\partial \sigma_{0V}}{\partial \boldsymbol{\varepsilon}_V^{\Pi}}\Big|_{\underbrace{u_z}_{rel.}} \dot{\boldsymbol{\varepsilon}}_V^{\Pi} = \left[\mathbb{C}_V^{ep}{}_{0\,0}^{\,0\,0}(z)\mathbb{P}_V^{\star}{}_{\,0}^{\,0}(z) + \frac{\mathbf{C}_V^{ep}{}_{0\,z}^{\,0\,z}(z)}{C_V^{ep}{}_{z\,z}(z)} \otimes \left(-\left(\mathbb{P}_V^{\star}{}_{\,0}^{\,0}\right)^T \mathbf{C}_V^{ep}{}_{z\,0}(z) + \frac{\mu_t}{\delta_t} C_t^{ep}\,\mathscr{V}\right)\right]\dot{\boldsymbol{\varepsilon}}_V^{\Pi} \tag{69}$$

The rate problem is completely solved once $\dot{\delta}_t$ is known from Eq. (63), since Equation (59) provides:

$$\dot{\varepsilon}_z(z) = \frac{1}{C_V^{ep}{}_{z\,z}(z)}\left(-\left(\mathbb{P}_V^{\star}{}_{\,0}^{\,0}\right)^T \mathbf{C}_V^{ep}{}_{z\,0}(z) + \frac{\mu_t}{\delta_t} C_t^{ep}\,\mathscr{V}\right)\cdot\dot{\boldsymbol{\varepsilon}}_V^{\Pi} \tag{64}$$

and the primary unknown field $\dot{u}_z(z)$ is computed taking the integral of (64) in the interval $[0, z]$, viz.:

$$\begin{aligned}\dot{u}_z(z) &= \dot{u}_z(0) + \int_0^z \frac{\partial \dot{u}_z}{\partial z}\,dz \\ &= \dot{u}_z(0) + \frac{\mu_t}{\delta_t} C_t^{ep} \int_0^z \frac{1}{C_V^{ep}{}_{z\,z}(z)}\,\mathscr{V}\,dz - \int_0^z \frac{1}{C_V^{ep}{}_{z\,z}(z)}\left(\mathbb{P}_V^{\star}{}_{\,0}^{\,0}\right)^T \mathbf{C}_V^{ep}{}_{z\,0}(z)dz\cdot\dot{\boldsymbol{\varepsilon}}_V^{\Pi}\end{aligned} \tag{65}$$

For the exterior unconfined layers undergoing plane stress conditions, Π_u^- and Π_u^+, the integrand in (68) is computed with the plane-stress elasto-plastic tangent operator.

Finally, considering the split $\Pi_c = \Pi_u^- \cup \Pi_u^+$ and additivity of integration, the tangent operator $\mathbb{H}_V$ of the TTJ chord, as determined by Equations (54) and (55), can be computed as the sum of the tangent operators $\mathbb{H}_V^C$ and $\mathbb{H}_V^U$ associated with the confined and unconfined region, respectively, viz.:

$$\mathbb{H}_V = \mathbb{H}_V^C + \mathbb{H}_V^U. \tag{70}$$

Substitution of Equation (69) in (68) provides a particularly compact expression of the tangent operator $\mathbb{H}_V^C$ of the confined core:

$$\mathbb{H}_V^C = \int_{z_c^-}^{z_c^+} \left(\overset{0}{\mathbb{P}}{}_V^{\star}\right)^T \overset{0\,0}{\mathbb{C}}{}_V^{ep}(z)\,\overset{0}{\mathbb{P}}{}_V^{\star}(z)\,dz + - \int_{z_c^-}^{z_c^+} \left(\overset{0}{\mathbb{P}}{}_V^{\star}\right)^T \frac{\overset{0\,z}{\mathbf{C}}{}_V^{ep}(z)}{\overset{z\,z}{C}{}_V^{ep}(z)} \otimes \left[\left(\overset{0}{\mathbb{P}}{}_V^{\star}\right)^T \overset{z\,0}{\mathbf{C}}{}_V^{ep}(z) - \frac{\mu_t}{\delta_t} C_t^{ep}\,\mathscr{V}\right] dz \tag{71}$$

Note that the first integral in Eq. (71) represents the tangent operator of the classical ESL-FSDT shell formulation which is independent of the transverse confinement. Actually, this term depends on the 5×5 submatrix $\overset{0\,0}{\mathbb{C}}{}_V^{ep}$ of the tangent operator of the core material (independent from ε_z), and on the (constant) geometric projector $\overset{0}{\mathbb{P}}{}_V^{\star}$. Conversely, the second integral computes the contribution of the TT confinement to the generalized tangent operator of the shell chord. In turn, this second term depends on $\overset{z\,0}{\mathbf{C}}{}_V^{ep}$ and $\overset{0\,z}{\mathbf{C}}{}_V^{ep}$, i.e. the z components of the material tangent operator, on the transverse ties stiffness C_t^{ep}, geometry and TT area ratio μ_t.

The second addend $\mathbb{H}_V^U$ in (70) is provided by

$$\mathbb{H}_V^U = \int_{z_c^-}^{z_c^+} \left(\mathbb{P}_V^{\star}\right)^T \left[\mathbb{C}_V^{ep}\,0\,0 - \frac{1}{C_V^{ep}\,z\,z}\mathbf{C}_V^{ep}\,z\,0 \otimes \mathbf{C}_V^{ep}\,z\,0\right] \mathbb{P}_V^{\star}(z)\,dz, \tag{72}$$

where the tensor under square bracket achieves the classical form of the elasto-plastic tangent operator obtained by stress condensation in case of plane stress [20,21].

Finally, it is worth being observed how the two limit behaviors of plane stress and zero TT stretch are consistently recovered by the proposed TTJ model, respectively for $\mu_t \to 0$ and $\mu_t \to \infty$. Specifically, whenever ties area is nil ($\Omega_t = 0$), so that $\mu_t = 0$, the second addend in Equation (55) vanishes together with the stress field $\sigma_z(z)$. Moreover, the second addend in square brackets in the second integral on the RHS of Equation (71) vanishes as well, so that the tangent operator assumes the classic plane-stress form entering (72). On the contrary, in the limit $\Omega_t \to \infty$, the terms $\mathscr{V}$ and $\dot{\delta}_t$ vanish due to Equations (62) and (63). In such case, Equation (65) yields for $z \in [z_c^-, z_c^+]$:

$$\dot{u}_z(z) = \dot{u}_z(0) + \int_0^z \frac{\partial \dot{u}_z}{\partial z}\,dz = \dot{u}_z(0) \tag{73}$$

what corresponds to the vertical displacement rate $\dot{u}_z(z)$ equal to its mid-plane value, throughout the core layer, with zero TT stretch. In presence of in-plane loading and when the chord is entirely confined ($z_c^- = -\delta/2$, $z_c^+ = \delta/2$ this condition corresponds to plane strain.

3. Numerical applications

In this section numerical applications are presented in order to

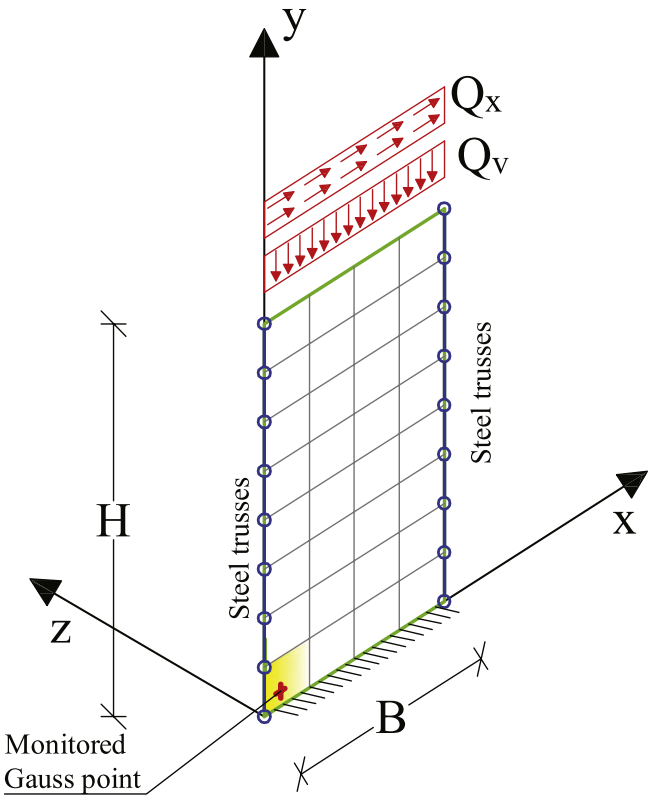

Fig. 3. Structural scheme of wall subject to in-plane pushover test.

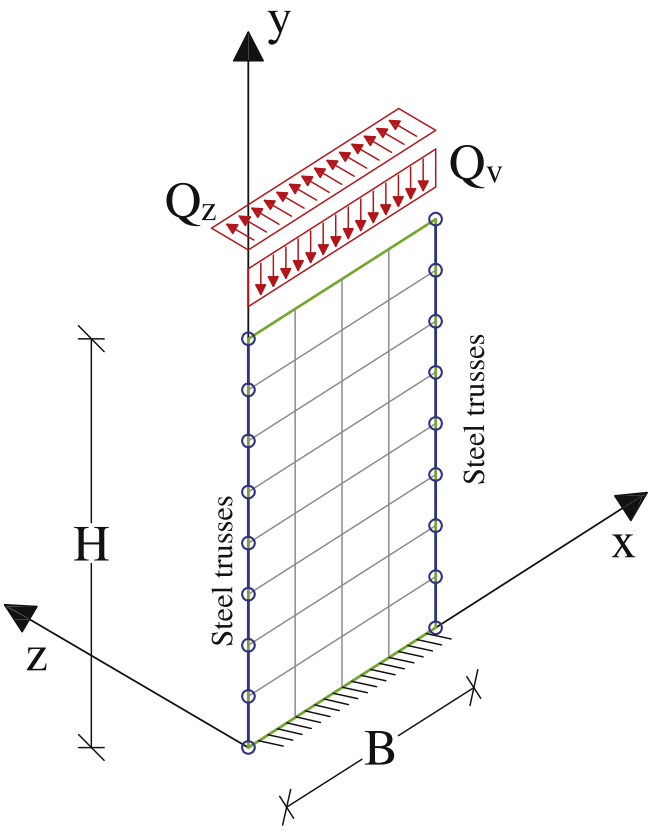

Fig. 4. Structural scheme of wall subject to out-of-plane pushover test.

illustrate the modeling features provided by the TTJS formulation detailed in Section 2. The effect of transverse confinement is examined in terms of global response and of local triaxial stress and strain states for two selected structural examples; they consist of rectangular walls fully clamped at the base subject to in-plane and out-of-plane pushover loading with geometry and loading parameters shown in Figs. 3 and 4.

Finite Element (FE) analyses have been carried out employing the 4-noded, 24 DOFs Mindlin-Reissner plate based MITC shell element formulation [48] for interpolating the generalized displacement fields $\mathbf{u}^{(m)}$ and $\boldsymbol{\beta}$ over the wall midplanes.

Analyses have been performed in the open-source object-oriented FEM code OpenSees [52], upon implementing the formulation for the TTJ chord presented in Section 2 as a user-defined section object-class. Given the generalized strain at each integration point of a shell element, the object-class computes the corresponding generalized stress and tangent operator.

Homogeneous elasto-plastic constitutive laws having the form described in Section 2.2 have been considered for all tests. In particular, an isotropic linear elastic-perfectly plastic behavior has been assumed for the reinforced core material of the wall; TT reinforcement area ratio as uniformly distributed over the shell mid-plane. The Young's modulus E and the Poisson's ratio ν, together with the yield function coefficients a, b, c, d entering (13), do not vary with x and y and, over the shell chord, along z. The shell chord is assumed to be entirely confined, i.e., $z_c^- = -\delta/2$, $z_c^+ = \delta/2$.

Transverse ties have been modeled employing the uniaxial Giuffré-Menegotto-Pinto [61] elasto-plastic model. This model has been selected since it is available in Opensees and it is endowed with an asymptotic hardening branch exhibiting a smooth yield transition which, by providing a convenient regularization of an ideal elastic-perfectly plastic uniaxial law, turned out to be also beneficial for numerical convergence. Furthermore, a no-compression behavior is added to TT reinforcement to reproduce a no-tension response of concrete in the TT direction in presence of TT shrinking of the shell core. This choice implies that $\sigma_z \leq 0$ in all simulations.

Both a J_2 and a Drucker-Prager yield function have been employed in the analyses since they approximate a large class of material responses encompassing both equal and differentiated tensile and compressive strengths, the Drucker-Prager model providing also a conveniently simple description of frictional materials.

Shell elements with 4 Gauss points have been considered. Shell chords located at the Gauss points have been further partitioned into 10 layers, each layer having its own elasto-plastic history variables integrated at each loading step. The TT integration points are located at the layer thickness midpoint. In all analyses a regular mesh of 4×8 quadrilateral elements have been used by considering nodes at the lower base of the wall fully constrained. We do not document the results of numerical examples referred to irregular meshes since insensitivity of the proposed layered TTJ-MITC shell element to mesh distortion is basically inherited from the underlying MITC formulation.

Our main concern was to evaluate the sensitivity of the global and local response to confinement by making the confinement ratio μ_t span the entire range $[0, +\infty[$ for every combination of in-plane/out-of-plane loading and J_2/Drucker-Prager yield functions. The results of these sensitivity analyses are reported in Section 3.2.

A second main objective of the analyses was to assess that the present formulation correctly fulfilled consistency with limit behaviors of the model associated with $\mu_t = 0$, i.e. a plane stress response, and $\mu_t = \infty$ corresponding to zero TT stretch.

Furthermore, as a first assessment of the predictive capabilities of the TTJS, we have documented in Section 3.3 the strength increment in RC walls induced by TT confinement assigned in accordance with Eurocode 2 provisions [62]. The numerical-experimental comparison has been purposefully carried out for RC structures in consideration of the higher degree of confidence/control of material properties guaranteed by code regulations and of the relevance of TT confinement in RC structural members.

The analyses on strength increment in RC walls motivated the choice of employing, for the elastic moduli and uniaxial strength, ordinary values prescribed by regulations for common design practices of RC members. Specifically, the constitutive parameters employed for concrete and reinforcement steel refer to class C20/25 and 450 of Eurocode 2 [62], respectively. Vertical load Q_v has been assumed to be twice the dead load of the wall in order to forfeitly account for vertical loads transferred by other structural members.

Early collapse of the wall due to tensile stress was prevented by the addition, along the vertical sides of the wall, of two vertical alignments of reinforcing uniaxial 2-noded steel trusses, as shown in Figs. 3 and 4. Trusses are modeled with the same constitutive law and parameters of the transverse ties with an area of 1885 mm^2 corresponding to $6 \times \phi 20$ mm.

The employed material and geometrical parameters are reported in Table 1.

Fig. 5 shows the biaxial elastic domains corresponding to the employed strength parameters for J_2 and Drucker-Prager yield functions. Due to the assumed values for the tensile and compressive uniaxial strengths for the Drucker Prager model, the biaxial elastic domain is unbounded in the direction of equibiaxial compression.

3.1. Geometry, loads and analysis specifications

The static pushover analyses consist of two loading steps. In the first step, vertical loads are applied by a linear ramp law up to a final compressive force $Q_v \cdot B = -400$ kN uniformly distributed on the

Table 1
Employed material and geometrical parameters for shell core and TT reinforcement common to all numerical analyses.

Description	Symbol	Units	Value
TT reinf. yield stress	$f_{y\,t}$	MPa	450
TT reinf.Young modulus	E_t	GPa	200
TT reinf. kinematic hardening modulus	H_t	GPa	20
Shell core Young modulus	E	GPa	21
Shell core Poisson ratio	ν	–	0.2
Shell core J_2 uniaxial strength	σ_y	MPa	25
Shell core Drucker-Prager uniaxial tensile strength	σ_{y+}	MPa	1.19
Shell core Drucker-Prager uniaxial compressive strength	σ_{y-}	MPa	−25
Wall height	H	m	4
Wall base width	B	m	2
Wall thickness	δ	m	0.5

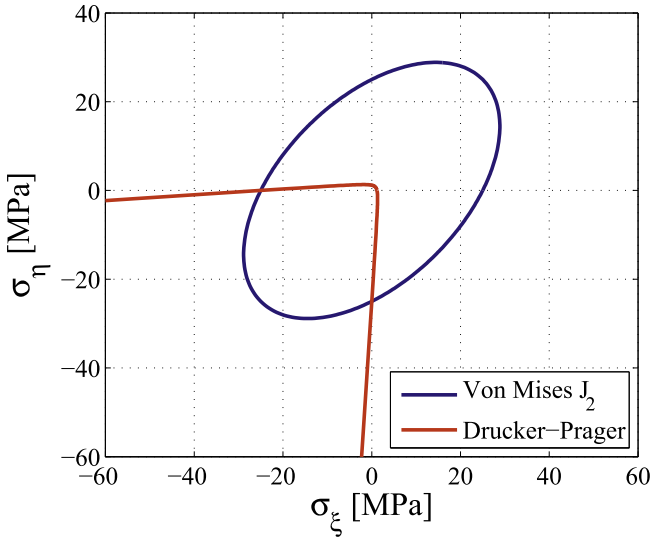

Fig. 5. Intersections of J_2 and Drucker-Prager yield domains with plane $\sigma_\zeta = 0$.

upper base of the wall. In the second step vertical loads are kept constant while horizontal loads are uniformly applied over the upper base and increased by means of a displacement driven control algorithm monitoring the horizontal displacement of the node at the middle-point of the upper base. In all analyses, displacements are increased up to 0.08 *m*, a value which is the 2% of the wall height.

Figs. 3 and 4 show the horizontal loads applied along *x* and *z*, activating in-plane membrane and out-of-plane flexural behavior in the wall, respectively.

3.2. Results of sensitivity analyses

A first set of numerical simulations was carried out to analyze the sensitivity of the wall response to the value of ties area ratio μ_t in relation to the employed yield criterion and to the in-plane/out-of-plane horizontal loading.

The response of the wall is examined in Section 3.2.1 in terms of global structural response, in Section 3.2.2 in terms of distribution of TT confining stress over the shell midplane and in Section 3.2.3 in terms of evolution of the local triaxial stress state at a selected monitored point of the structure.

3.2.1. Load-displacement curves

Fig. 6 shows two families of load-displacement R_x-U_x curves, where $R_x = B \cdot Q_x$ is the total horizontal load and U_x is the *x* displacement component of the top-middle point of the wall, computed during the shear step of the pushover loading. This family of curves is obtained at different values of μ_t including $\mu_t = 0$ and $\mu_t = \infty$, where the latter value has been enforced by directly setting the zero TT-stretch $\varepsilon_z = 0$ at all integration points of the shells.

Fig. 6(a) reports the results obtained with the J_2 yield surface and Fig. 6(b) refers to the Drucker-Prager yield surface.

As expected, for a given value of shear displacement, the structure gains stiffness and reaches higher shear loads as μ_t increases. More interestingly, numerical results show that the curves corresponding to plane stress ($\mu_t = 0$) and zero TT-stretch ($\mu_t = \infty$) bound all other structural responses obtained at intermediate μ_t values, thus confirming the analytical considerations of limit plane-stress and zero TT stretch conditions made in Section 2. In both Fig. 6(a) and (b) the nonlinear shapes of the curves show that during shearing the elastic regime is exceeded in all simulations.

The load-displacement curves corresponding to out-of-plane loading are plotted in Fig. 7 with the same layout of Fig. 6. The plotted variables are the total horizontal load along *z*, $R_z = B \cdot Q_z$ and the displacement U_z of the top-middle point of the wall. Also in this case plane stress and zero TT stretch limits bound all $R_z - U_z$ curves. It can be observed from Fig. 7(a) that, when J_2 plasticity is considered, effects of TT confinement are absent since all curves overlap.

For out-of-plane bending with J_2 plasticity, numerical results showed that one has uniformly $\sigma_z = 0$, through the whole panel and during all time steps. This circumstance is easily explained by considering that, in out-of-plane flexure, the vertical stress and the deformation over the shell chord are antisymmetric with respect to the middle plane, see, e.g., 'Fig. 10(c); hence the mean thickness elongation (i.e., the variation of δ_t) due to bending is zero and the out-of-plane flexural behavior is uncoupled from σ_z.

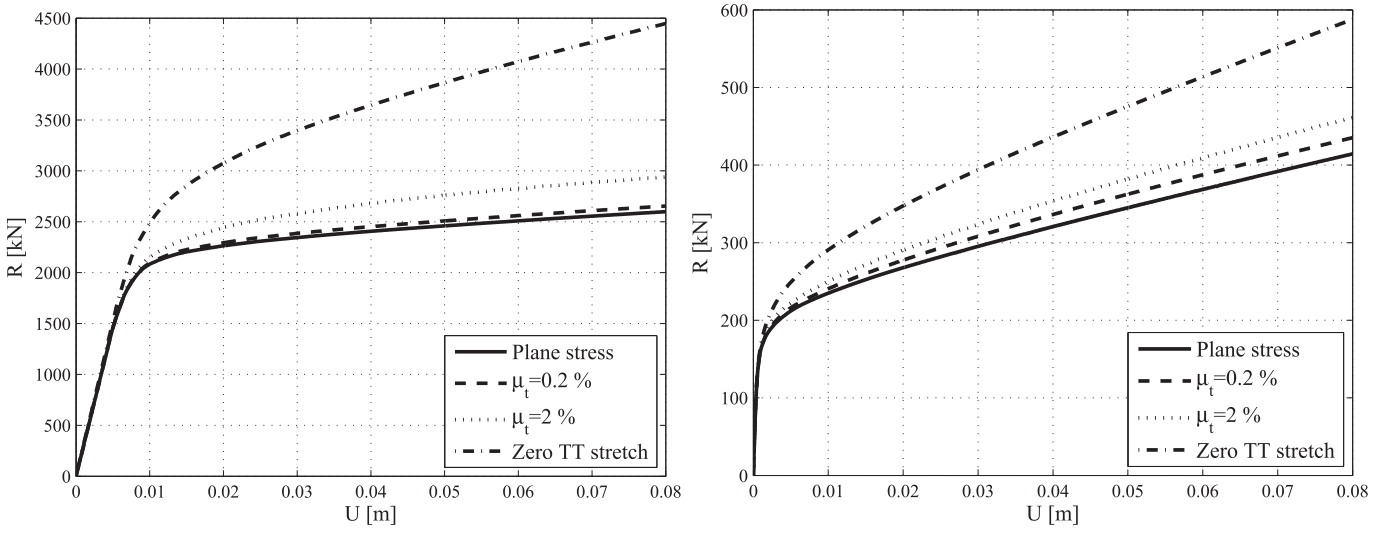

(a) J_2 core (b) Drucker-Prager core

Fig. 6. Wall subject to in-plane pushover – Load-Displacement curves.

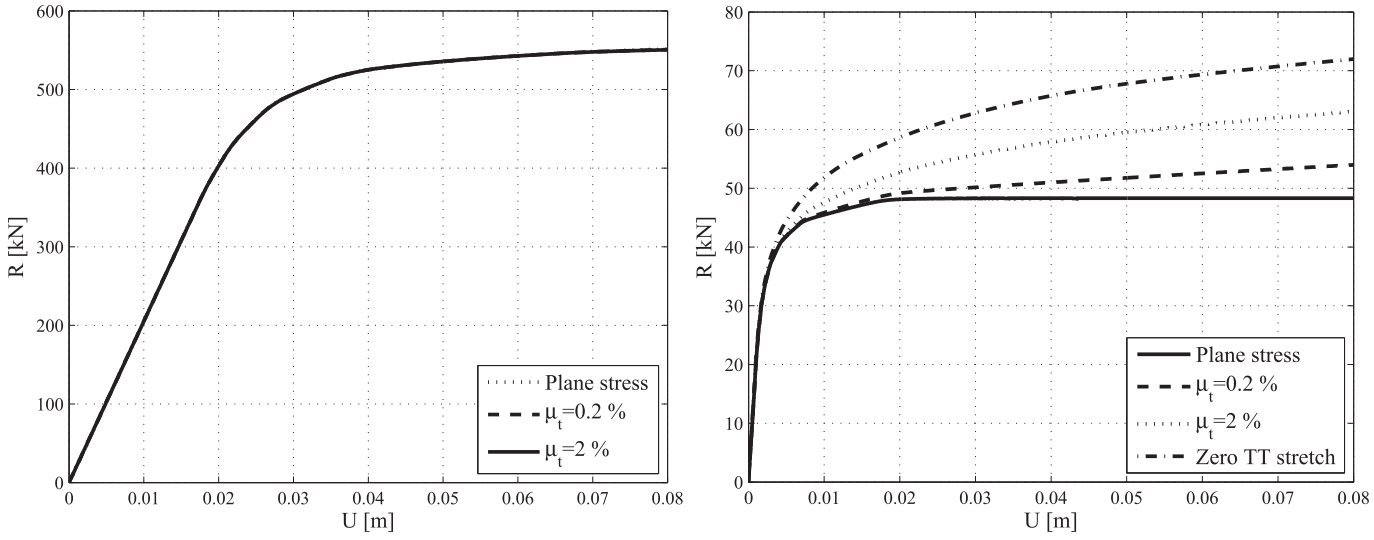

(a) J_2 core (b) Drucker-Prager core

Fig. 7. Wall subject to out-of-plane pushover – Load-Displacement curves.

The same effect is not detected with Drucker Prager plasticity since the different tensile and compressive elasto-plastic behavior disrupts the middle-plane antisymmetry inducing coupling with σ_z and a consequent sensitivity to confinement; this is shown in Fig. 7(b) where a more pronounced stiffness increment with increasing μ_t is observed. This effect is due to the pure-bending, sketched in Fig. 10(d), induced by the mutual magnitude of axial force and bending moment. Thus, the neutral axis of the monitored Gauss point does not belong to the middle plane of the shell.

3.2.2. Distribution of TT confinement stress

Figs. 8–10 report the colormap contours of σ_z, plotted over the deformed shape of the rectangular panels, corresponding to the last step of the pushover analyses, i.e. at the maximum horizontal displacement $U = 0.08\ m$. Stresses are plotted for all loading/yield criteria combinations (except for the J_2 case where, as above reported, the analyses yield uniformly $\sigma_z = 0$) and at different TT reinforcement area ratios.

All contours show the increase of confining stress σ_z with μ_t. Moreover, white areas correspond to regions where $\sigma_z = 0$. This condition is the result of the previously described tensile–only constitutive model of the ties, and substantially corresponds to concrete shrinking in z direction.

The computed confining stress distributions consistently reflect the distribution of TT stretch which would be more simply analytically evaluated by a cantilever model subjected to combined axial force and uniaxial in-plane and out-of-plane flexure. In particular, in Fig. 8(a) and (b) the region with compressive σ_z at the wall base essentially corresponds to the left half of the structure. Actually, the neutral axis at the clamped end section is parallel to axis z and, due to the high eccentricity of stress resultants at the base section, is located almost at the middle point of the base so that the left half of the wall is compressed and the right half is subject to tensile actions. This is consistent with the relative magnitude of axial vertical force and bending at the base section for which the wall is subject to almost–pure bending.

In case of zero TT stretch (Fig. 8(c)), the onset of confining compressive stresses is observed to have a broader distribution involving the right side of the wall with the presence of 45°-inclined purple region. This is indicative of the presence of a compressed region inducing compressive σ_z as a consequence of the transverse dilation impeded by the zero TT stretch hypothesis.

A similar distribution of confinement stress is found in the tests where shells are modeled by the Drucker-Prager yield criterion

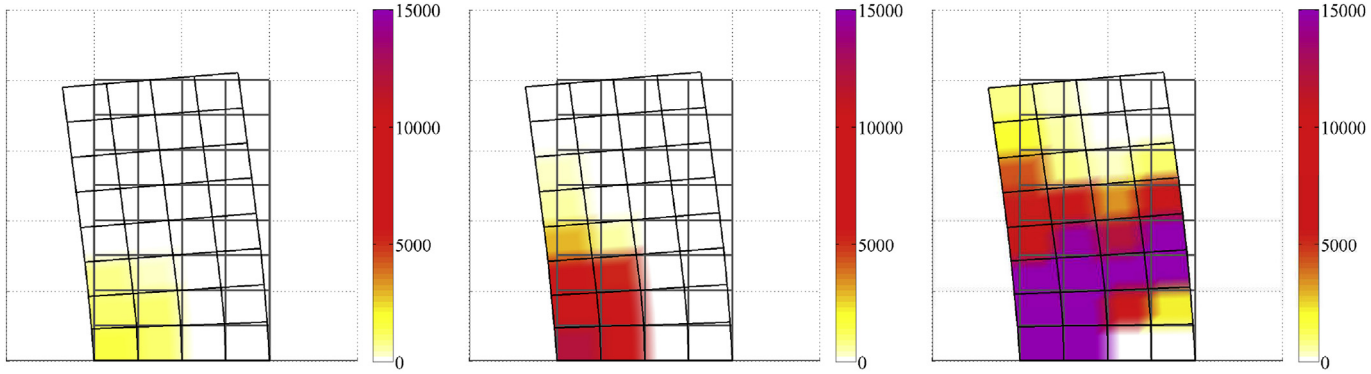

(a) μ_t = 0.2% (b) μ_t = 2.0% (c) $\mu_t = \infty$

Fig. 8. Colormap contours of compressive TT confinement stress ($-\sigma_z$, [kPa]) – In-plane pushover test – J_2 core (Deformed shape out of scale).

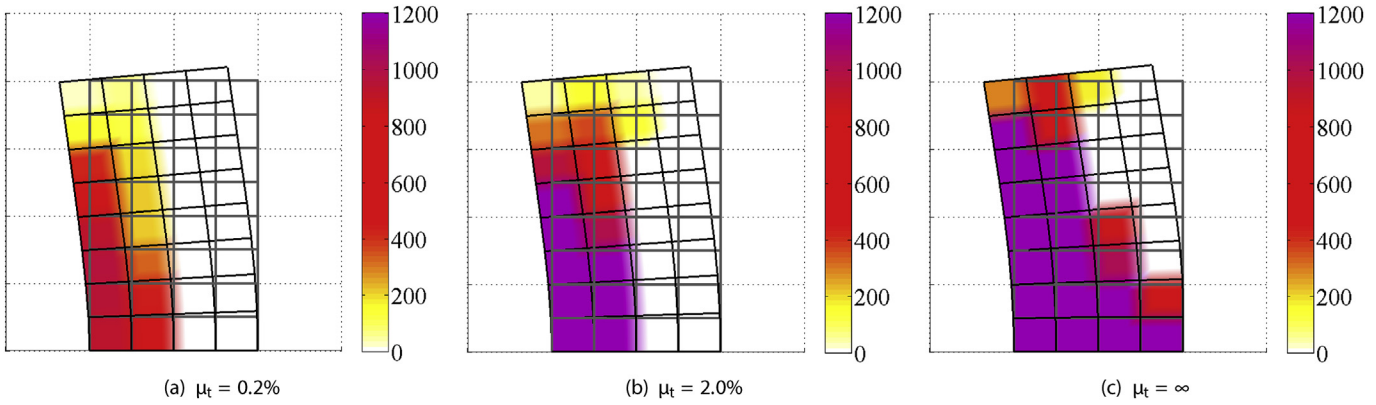

Fig. 9. Colormap contours of compressive TT confinement stress ($-\sigma_z$, [kPa]) – In-plane pushover test – Drucker-Prager core (Deformed shape out of scale).

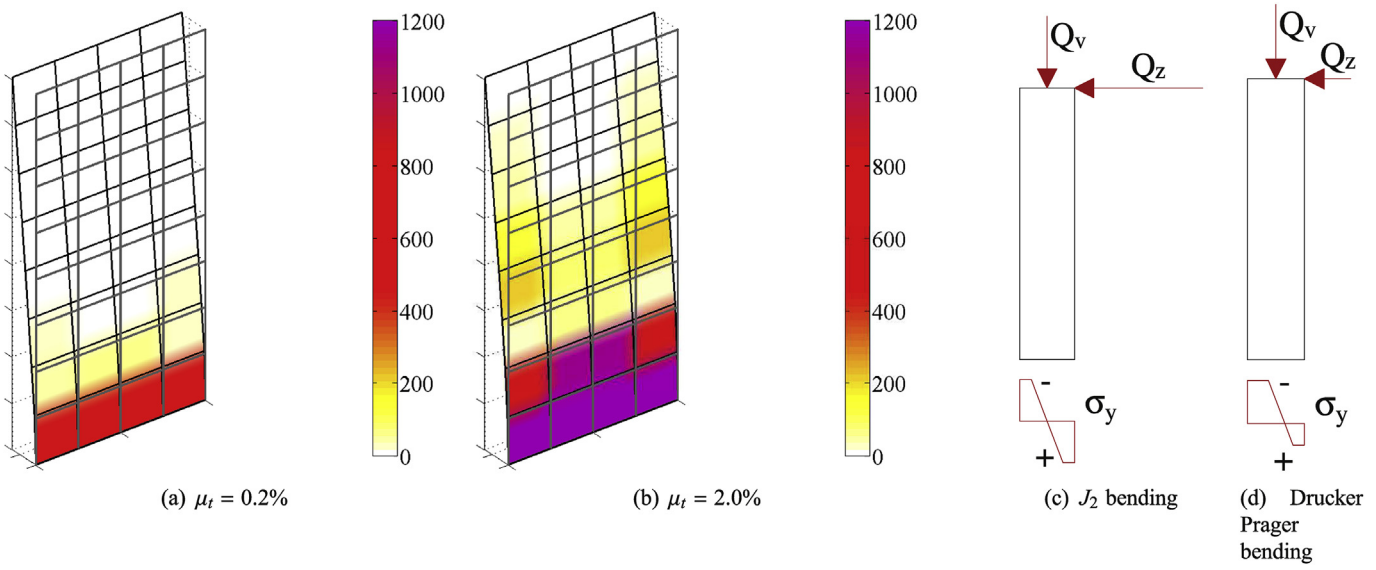

Fig. 10. Colormap contours of compressive TT confinement stress ($-\sigma_z$, [kPa]) – Out-of-plane pushover test – Drucker-Prager core (Deformed shape out of scale) and bending schemes.

plotted in Fig. 9. The order of magnitude of confinement stress results lower since the Drucker-Prager wall stiffness is lower than the J_2 one; thus, at a same value of the horizontal displacement, stresses are expected to be lower.

Results of out-of-plane pushover test with shells modeled by Drucker-Prager material are illustrated in Fig. 10(a) and (b). Results with the J_2 material are not plotted since, as previously observed, the computed TT confining stress σ_z is zero due to the anti-symmetry of deformation with respect to the middle plane, see, e.g., Fig. 10(c). On the contrary, when the Drucker-Prager law is employed, the stress resultants at the base section, consisting in coupled compressive axial force and uniaxial out-of-plane bending, produce an unsymmetrical stress distribution, sketched in Fig. 10(d), which induces a positive TT elongation which ultimately results into TT confining stress reaction.

3.2.3. Local triaxial stress state evolution

The response of the wall to in–plane pushover loading is examined in closer detail in terms of evolution of the local triaxial stress state. This is monitored at the chord associated with the Gauss point indicated in Fig. 3, in particular at the integration point located at the shell middle plane, i.e., at $z = 0$. However, since in the in–plane test internal actions are limited to membrane behavior, the selected integration point is representative of the behavior of the whole chord.

Results concerning pushover analyses with both the J_2 and the Drucker-Prager criteria are hereby reported by plotting the evolution curves of the monitored stress tensor in the space of principal stresses. In particular, a family of evolution curves is generated for different values of μ_t and comparing the response with curves corresponding to perfect plane-stress and zero TT-stretch conditions.

The response obtained with the J_2 criterion is shown in Fig. 11. The yellow cylinder represents the J_2 yield surface while the red plane is the locus corresponding to plane stress behavior (i.e., with $\sigma_\zeta = 0$). The black-dashed line is the hydrostatic axis for which $\sigma_\xi = \sigma_\eta = \sigma_\zeta$, while the black-solid line is the elliptical intersection between the yield surface and the plane $\sigma_\zeta = 0$. Depicted curves, computed for different values of ties area ratio, represent the evolution of principal stress components during the in-plane test.

The plane stress response, recovered by setting $\mu_t = 0$ in the structural model, corresponds to the blue line. In this curve, as expected, principal stresses remain contained within plane $\sigma_\zeta = 0$ and the plastic branch follows the biaxial yield ellipse.

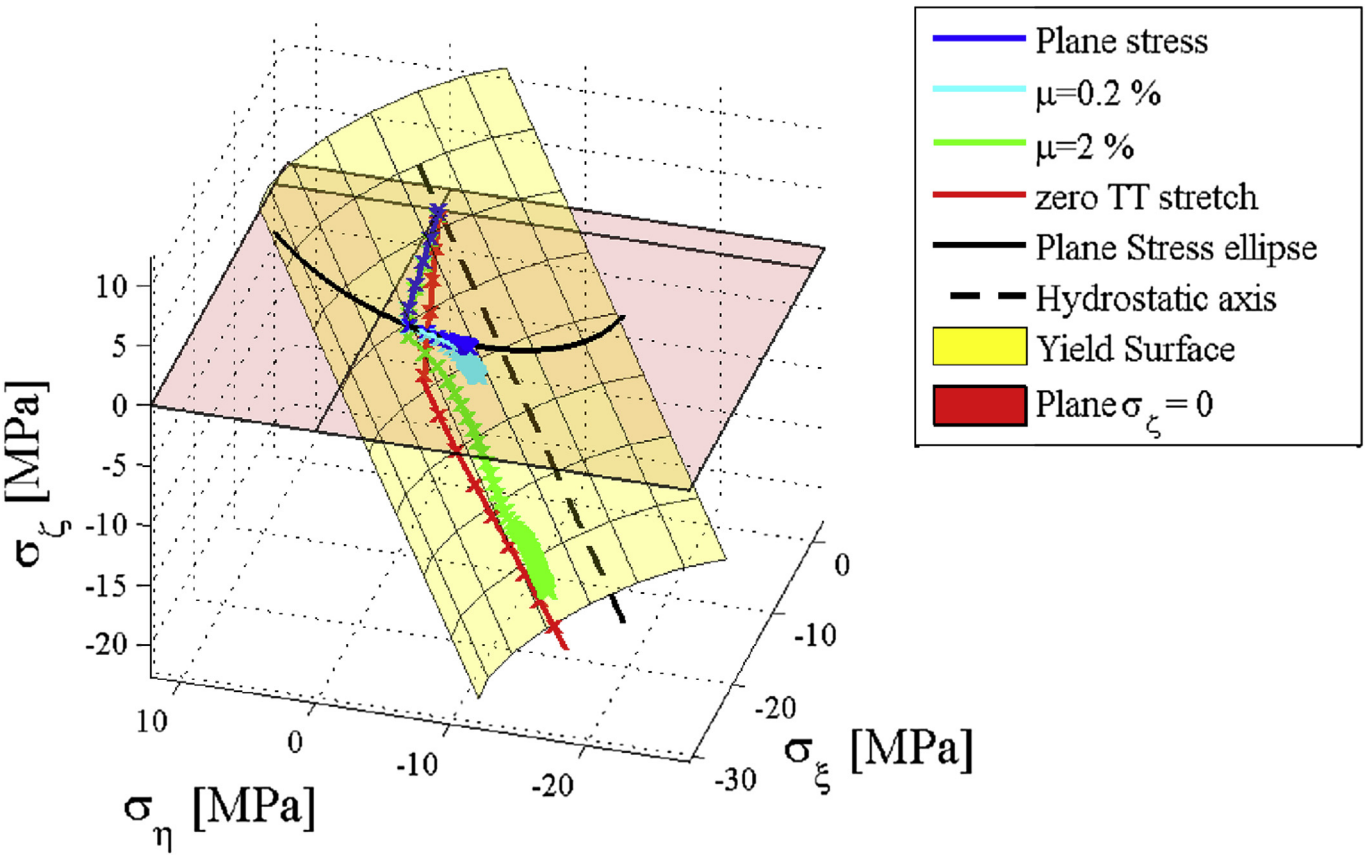

Fig. 11. Yield surface and principal stress path – in-plane pushover test, J_2 shells.

Transversal confinement produces two effects which can be observed in the figure. During the elastic phase the slope of the stress paths increases with the ties area ratio as well as the yield stress; however such a phenomenon is not prominent. A significantly more pronounced effect is observed for nonzero μ_t in the plastic branches of these curves, confined onto the boundary of the constant J_2 cylindrical yield surface. These branches depart from the $\sigma_\zeta = 0$ plane, and drift towards the hydrostatic axis. In particular, it is noticeable how the propagation of green and red curves, corresponding to $\mu_t = 2\%$ and plane strain, respectively, tends to run parallel to the hydrostatic axis. This peculiarity indicates of course that the increasing load results in an increment of the spherical part of the stress tensor while the deviatoric part remains constant in norm.

Fig. 12(a) reports the corresponding results for the Drucker-Prager yield surface with the same layout of Fig. 11, showing the known increased beneficial effect of confinement for this criterion dependent upon the first two stress invariants. Fig. 12(b) shows an alternative plot of the stress paths where the deviatoric part of the stress D is plotted vs. the spherical one S.

3.3. Evaluation of TT confinement-induced strength increment in RC walls

To explore the applicability of the TTJS formulation in civil engineering analyses, this section estimates the increment range of strength induced by transverse confinement for the structural wall considered in Fig. 3. The strength increment is hereby estimated by a straightforward adoption of Eurocode 2 provisions [62] for beam element design. Specifically, the strength increment of the wall subject to in–plane pushover is determined by identifying the attainment of the ultimate limit state and, in particular, considering the increment of limit stress and strain for confinement effects proposed in chapter 3.1.9 of Eurocode 2 provisions.

To this end the interaction between TT reinforcement in RC walls and the concrete core is assumed to be described by the kinematic hypotheses of Section 2.5, i.e., with TT reinforcement and concrete core being able to deform undergoing independent TT stretches. For concrete the Drucker-Prager law is employed using again the parameters of Table 1 referred to a class C20/25 concrete. A $\mu_t = 0.2\%$ TT area ratio is employed as a value representative of a TT reinforcement corresponding to $\phi 10\,mm$ steel ties with spacing $0.2 \times 0.2\,m$. Sensitivity of strength estimates to increasing μ_t has also been explored.

The provision accounting for the effect of confinement in RC members (Chapter 3.1.9 in Ref. [62]), prescribe the following correlations between the confined ultimate strain $\varepsilon_{cu2,c}$ and the confinement stress, σ_z

$$\varepsilon_{cu2,c} = \varepsilon_{cu2} + 0.0002\frac{\sigma_z}{f_{ck}}, \tag{74}$$

where ε_{cu2} is the ultimate limit strain and f_{ck} is the (unconfined) cylindrical limit stress of concrete. Similarly, the correlation for the concrete confined strength $f_{ck,c}$ provided by Eurocode 2 reads:

$$f_{ck,c} = f_{ck}\left(1 + 5\frac{\sigma_z}{f_{ck}}\right) \tag{75}$$

In particular, for the considered class of concrete one has $f_{ck} = -25MPa$ and $\varepsilon_{cu2} = 0.0035$.

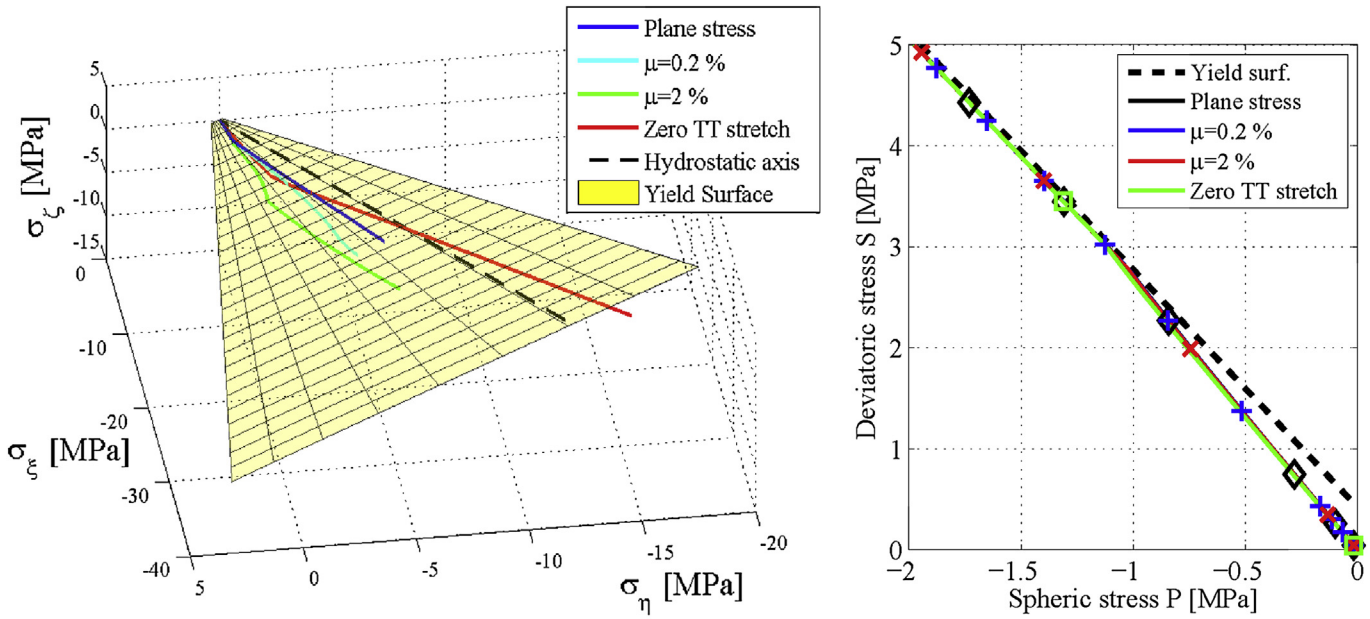

(a) Yield surface and principal stress path (b) Deviatoric vs. Spherical stress

Fig. 12. Yield surface and principal stress path – in-plane pushover test, Drucker-Prager shells.

Ultimate strength of the RC panel is conventionally identified by Eurocode 2 with the first attainment of the value $\varepsilon_{cu2,c}$ for the longitudinal strain, referred to beam elements. By identifying the longitudinal direction with axis *y*, the strain component ε_y is taken for the longitudinal strain. The most stressed shell element is depicted in yellow in Fig. 3 for the in-plane pushover test.

It is worth being emphasized that the presence of confining ties has two different effects on the behavior of the core material. The spheric stress increment determined by increased values of μ_t shifts the attainment of the yield surface towards higher values of principal stresses for a same given deformation level. Furthermore, the nonzero value of σ_z, according to Equation (74), results in an increment of $\varepsilon_{cu2,c}$. Although small, this increment significantly increases the top horizontal displacement of the wall corresponding to the attainment of the ultimate limit state for concrete at the wall base section.

Confinement stress σ_z is directly computed by the FE structural analysis. Fig. 13(a) shows, for several values of μ_t, the curves obtained plotting vertical strain vs. σ_z as function of μ_t. The gain in ultimate limit strain $\varepsilon_{cu2,c}$ provided by Equation (74) is represented by the dashed line. Intersections of solid and dashed lines, denoted by diamond markers, correspond to the attainment of the ultimate limit state for concrete at different TT reinforcement area ratios Indeed, for $\mu_t = 0.2\%$, the ultimate load increases of:

$$\Delta = \frac{R^{uls}_{\mu_t=0.2\%}}{R^{uls}_{\mu_t=0}} - 1 = 18\%. \tag{76}$$

Diamond markers also represent the attainment of ultimate limit states in Fig. 13(b) where the corresponding load-

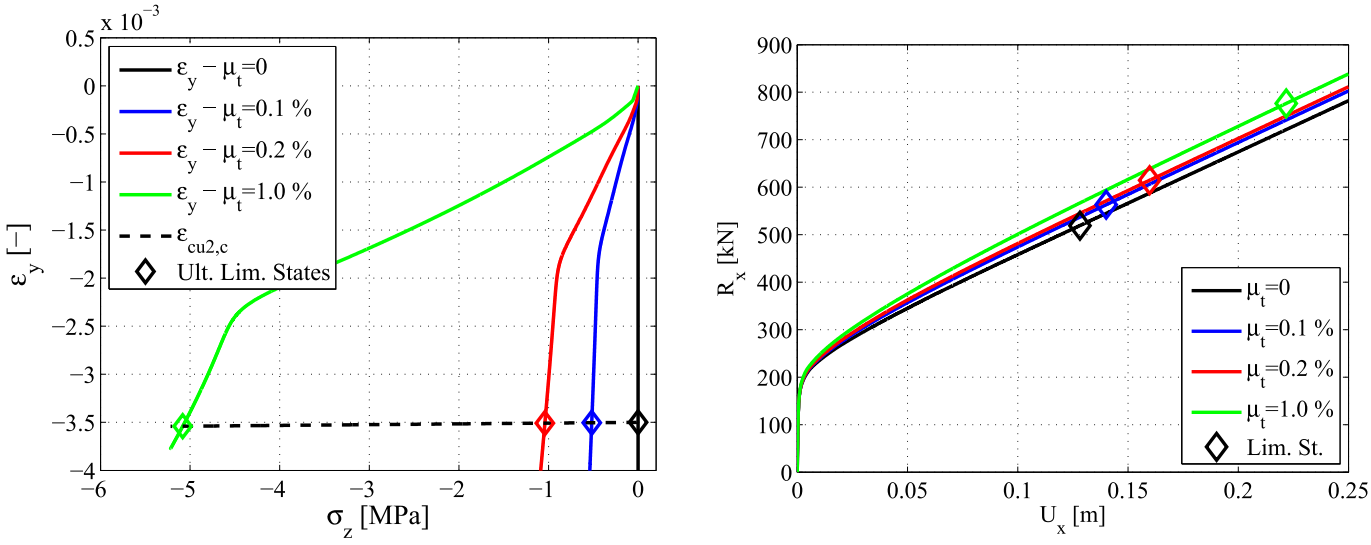

(a) Limit and vertical strain components vs. confinement stress σ_z (b) Load–displacement curves

Fig. 13. Drucker-Prager wall subject to in-plane pushover: strength increment estimation.

displacement ($U_x - R_x$) curves of the wall are plotted. This graph shows that, alongside with the strength increment captured by the triaxial TTJS analysis, the ultimate limit state is attained at larger horizontal displacements when μ_t is increased, i.e., the confinement effect modeled by Equation (74) is also associated with an increment of the wall ductility.

Strength increments show a similar order of magnitude if computed starting from Equation (75). In fact, the computed confinement stress, obtained from the finite element results at the ultimate limit state, turns out to be $\sigma_z = -1.0405\ MPa$; the concrete confined ultimate stress $f_{ck,c}$, provided by Equation (75), turns out to be

$$\frac{f_{ck,c}}{f_{ck}} - 1 = 20.81\%. \tag{77}$$

The recovery of physically plausible orders of magnitude for these strength increment estimates, which fall within the ranges of common practice design, provides an encouraging assessment of the structural analyses herein reported.

4. Conclusions

A generalized shell formulation for the triaxial stress analysis of Through-the-Thickness (TT) confining mechanisms induced by Through-the-Thickness Jacketing (TTJ) devices in laminated composite structures has been proposed.

By assuming a smeared description of TT reinforcements, the proposed formulation has been constructed as an enhancement of the classical laminated ESL-FSDT shell theory, capturing the TTJ interaction between transverse uniaxial reinforcements and confined layers in terms of continuum equilibrium and compatibility equations.

Statics and kinematics of the shell have been developed by following standard work-association arguments and encompassing both TT-laminated and TT-functionally graded structures.

Upon introducing elasto-plastic constitutive assumptions for the shell core and the reinforcements, a closed-form explicit representation of the consistent elasto-plastic tangent operator has been derived, thus allowing for return mapping algorithms with optimal convergence features within Newton-Raphson integration schemes. It has been analytically shown that the response predicted by the TTJ formulation is consistently bounded by the ordinary plane stress response and by the zero TT-stretch response, respectively recovered in the limits of vanishing TT reinforcement and infinitely stiff TT reinforcements.

The TTJ formulation has been subsequently combined with a 2D layered MITC shell finite element and exploited in the nonlinear FE simulation of in-plane and out-of-plane pushover tests for composite TT-reinforced rectangular panels. In particular, the proposed formulation represents a versatile tool to be combined with 3D elasto-plastic constitutive models for the shell core and shell finite element formulations.

These FE analyses have provided an assessment of the proposed modeling strategy in terms of both global predicted structural response and local triaxial response of the shell chords.

Results of the nonlinear structural analyses for TT confined panels subject to in-plane and out-of-plane pushover, endowed with a J_2 and Drucker-Prager elasto-plastic behavior of the shell core, indicate that the TTJ approach efficiently captures the confining interaction between the shell core and the TT reinforcement, while granting predictions that are physically meaningful and consistent with those provided by simpler analytical 1D models (albeit 1D models cannot capture confinement effects).

In particular, numerical results have confirmed that the responses corresponding to zero TT-stretch ($\mu_t = \infty$) and plane stress ($\mu_t = 0$), represent upper and lower bounds to the responses obtained at intermediate values of the reinforcement area ratio μ_t. These results have also shown the capability of the proposed modeling strategy to track a complex triaxial interaction between the shell core and the TT reinforcement along the TT shell chords. The computed interaction was found to determine a structurally relevant stress redistribution, both in the elastic and in post-elastic phases, resulting into marked global structural effects of increased stiffness, strength and ductility.

Altogether the above highlighted features indicate that the TTJS structural formulation introduces a new perspective in the 2D nonlinear structural stress analysis of composite shell structures retrofitted by ad-hoc transverse confinement devices. The kinematic hypotheses underlying the TTJS formulation are specifically suited for describing physical systems in which the interaction at the tie-core interface is loose or absent so that differential dilatations are permitted. Accordingly, examples of these structural typologies, where TTJS may find a convenient application for stress analysis, are masonry panels retrofitted by composite ribbons and TT jacketed concrete sandwich panels.

More interestingly, the results of simulations of out-of-plane pushover tests have shown that TTJS captures a beneficial and structurally significant effect of TT confinement even for out-of-plane responses when an elasto-plastic constitutive behavior with different compressive and tensile strengths is employed. These constitutive assumptions are well suited for concrete and masonry walls.

A separate discussion deserves the application of the TTJS formulation for modeling the interaction between built-in stirrups and concrete core in ordinary RC walls. In these structural members the TT confining mechanism can be activated only when differential TT stretching are permitted between transverse steel bars and the surrounding concrete. It can be conjectured that such a differential TT stretch can be activated as a consequence of cracking in a way similar to tension stiffening. While this hypothesis requires an experimental corroboration, the numerical evaluations carried out in Section 3.3 have indicated that a straightforward application of Eurocode 2 provisions for estimating the strength increment, on the basis of the output data from 2D TTJ FE shell analyses of in-plane pushover tests on RC walls, yields approximately 20% strength increase when an ordinary stirrup reinforcement is considered.

Concerning the future developments of the present line of research, the direct continuation of this study will address the strategy for the numerical FE integration of the TTJS formulation and the related implementation issues in OpenSees.

Moreover, while the focus of the present study has been deliberately confined to the consideration of ideal associated elasto-plastic constitutive laws in order to explore the features of the mechanical response predicted by the TTJ formulation in the nonlinear range proceeding by an incremental approach, the use of the TTJ formulation combined with more refined constitutive and structural models suitably tailored for the description of quasi-brittle composite materials in civil structural engineering applications will be a future research endeavor. In particular, with a primary view towards the nonlinear seismic analysis of masonry and concrete walls, future research topics will be the combination of the TTJ formulation with plastic-damage models [63] and, more in general, the incorporation of friction, damage and unilateral contact in the constitutive response [64].

Although this study has been focused on plane structures, the TTJS formulation can be ordinarily applied to address curved structures, such as masonry vaults and domes, for which use of jacketing is also constitutes a viable retrofitting technique. Effects

of TT confinement will be investigated and compared with alternative computational strategies, such as tensegrity approaches [65,66] and thrust-surface-based procedures [67,68], in order to check the effectiveness of the proposed modeling strategy in presence of curved structural elements.

The TTJ formulation will be also employed in combination with the use of seismic response envelopes [69,70] and encompassing soil-structure interaction with Equivalent Foundation Oscillator [71], Winkler-Contact interfaces [72], fully 3D models [73] as well as with less-computationally expensive potential-based approaches [74,75].

Acknowledgements

This study was funded by Regione Campania and by European funds via the project: “Analisi numerica e prove sperimentali del comportamento di elementi strutturali in calcestruzzo armato soggetti a taglio e essione composta”, Legge 5 Campania - year 2007 (CUP: F82I15000100002).

References

[1] Mander JB, Priestley MJN, Park R. Theoretical stress–strain model for confined concrete. J Struct Eng 1988;114(8):1804–26.
[2] Borri A, Castori G, Corradi M. Masonry columns confined by steel fiber composite wraps. Materials 2011;4:311–26.
[3] Nisticó N. R.c. square sections confined by FRP: a numerical procedure for predicting stress-strain relationships. Compos Part B Eng 2014;59:238–47.
[4] Trapko T. Stress-strain model for FRCM confined concrete elements. Compos Part B Eng 2013;45(1):1351–9.
[5] Kang W-H, Kim J. Reliability-based flexural design models for concrete sandwich wall panels with continuous GFRP shear connectors. Compos Part B Eng 2016;89:340–51.
[6] Corradi M, Borri A, Castori G, Sisti R. Shear strengthening of wall panels through jacketing with cement mortar reinforced by GFRP grids. Compos Part B Eng 2014;64:33–42.
[7] Sharifi S, Gohari S, Sharifiteshnizi M, Vrcelj Z. Numerical and experimental study on mechanical strength of internally pressurized laminated woven composite shells incorporated with surface-bounded sensors. Compos Part B Eng 2016;94:224–37.
[8] Guinovart-Sanjuán D, Rodríguez-Ramos R, Guinovart-Díaz R, Bravo-Castillero J, Sabina F, Merodio J, et al. Effective properties of regular elastic laminated shell composite. Compos Part B Eng 2016;87:12–20.
[9] Palazzo V, Rosati L, Valoroso N. Solution procedures for J3 plasticity and viscoplasticity. Comput methods Appl Mech Eng 2001;191(8):903–39.
[10] Corradi M, Grazini A, Borri A. Confinement of brick masonry columns with CFRP materials. Compos Sci Technol 2007;57:1772–83.
[11] Ozbakkaloglu T, Lim JC. Axial compressive behavior of FRP-confined concrete: experimental test database and a new design-oriented model. Compos Part B Eng 2013;55:607–34.
[12] Berto L, Saetta A, Scotta R, Vitaliani R. An orthotropic damage model for masonry structures. Int J Numer Methods Eng 2002;55:127–57.
[13] Mirmiran A, Zagers K, Yuan W. Nonlinear finite element modeling of concrete confined by fiber composites. Finite Elem Analysis Des 2000;35(1):79–96.
[14] Krevaikas TD, Triantatillou TC. Masonry confinement with fiber–reinforced Polymers. J Compos Constr ASCE 2005;9(2):128–35.
[15] Ilyas M, Farooq SH, Qazi AU, Umair R. Masonry confinement using steel strips. Pak J Eng Appl Sci 2009;5:1–9.
[16] Cheng Y, Fan Y. Modeling of reinforcement in concrete and reinforcement confinement coefficient. Finite Elem Analysis Des 1993;13(4):271–84.
[17] Giuriani E, Plizzari G, Schumm C. Role of stirrups and residual tensile strength of cracked concrete on bond. J Struct Eng 1991;117(1):1–18.
[18] The European Union Per Regulation 305/2011. Bs en 1992:2004, eurocode 2: design of concrete structures. Tech. rep., The European Union; 2004.
[19] Minaie E, Moon FL, Hamid AA. Nonlinear finite element modeling of reinforced masonry shear walls for bidirectional loading response. Finite Elem Analysis Des 2014;84:44–53.
[20] Valoroso N, Rosati L. Consistent derivation of the constitutive algorithm for plane stress isotropic plasticity. Part I: theoretical formulation. Int J Solids Struct 2009;46(1):74–91.
[21] Valoroso N, Rosati L. Consistent derivation of the constitutive algorithm for plane stress isotropic plasticity. Part II: computational issues. Int J Solids Struct 2009;46(1):92–124.
[22] Mostofinejad D, Anaei MM. Ductility of confined concrete masonry shear walls. Bull N. Z Natl Soc Earthq Eng 1982;15(1):22–6.
[23] Choi K-B, Choi W-C, Feo L, Jang S-J, Yun H-D. In-plane shear behavior of insulated precast concrete sandwich panels reinforced with corrugated GFRP shear connectors. Compos Part B Eng 2015;79:419–29.
[24] Medani T, Liu X, Huurman M, Scarpas A, Molenaar A. Experimental and numerical characterization of a membrane material for orthotropic steel deck bridges: Part 1: experimental work and data interpretation. Finite Elem Analysis Des 2008;44(9–10):552–63.
[25] ACI Committee 318. Building code requirements for structural concrete (aci 318-08) and commentary. Tech. rep., American Concrete Institute; 2008.
[26] Valluzzi M, Da Porto F, Modena C. Behavior and modeling of strengthened three-leaf stone masonry walls. Mater Struct 2004;37(3):184–92.
[27] Oliveira DV, Silva RA, Garbin E, Lourenço PB. Strengthening of three-leaf stone masonry walls: an experimental research. Mater Struct 2012;45(8):1259–76.
[28] Pinho FF, Lúcio VJ, Baião MF. Rubble stone masonry walls strengthened by three-dimensional steel ties and textile-reinforced mortar render under compression and shear loads. Int J Archit Herit 2015;9(7):844–58.
[29] Mostofinejad D, Anaei MM. Effect of confining of boundary elements of slender RC shear wall by FRP composites and stirrups. Eng Struct 2012;41:1–13.
[30] S. Churilov, E. Dumova-Jovanoska, Analysis of masonry walls strengthened with RC jackets, in: Proc. 15th World Conference on Earthquake Engineering (WCEE), Lisboa, Portugal, 2012, pp. 1–10.
[31] Liu X, Medani T, Scarpas A, Huurman M, Molenaar A. Experimental and numerical characterization of a membrane material for orthotropic steel deck bridges: Part 2. Finite Elem Analysis Des 2008;44(9–10):580–94.
[32] Janaraj T, Dhanasekar M. Finite element analysis of the in-plane shear behaviour of masonry panels confined with reinforced grouted cores. Constr Build Mater 2014;65:495–506.
[33] T. Janaraj, M. Dhanasekar, Effectiveness of two forms of grouted reinforced confinement methods to hollow concrete masonry panels, J Mater Civ Eng 27(12).
[34] Reddy JN. Mechanics of laminated composite plates and shells: theory and analysis. second ed. Boca Raton, Fl, USA: CRC Press, Taylor & Francis Group; 2003.
[35] Green AE, Zerna W. The equilibrium of thin elastic shells. Q J Mech Appl Math 1950;3(1):9–22.
[36] Reissner E. On finite axi-symmetrical deformations of thin elastic shells of revolution. Comput Mech 1989;4(5):387–400.
[37] Simo J, Rifai M, Fox D. On a stress resultant geometrically exact shell model. Part IV: variable thickness shells with through-the-thickness stretching. Comput Methods Appl Mech Eng 1990;81(1):91–126.
[38] Buchter N, Ramm E, Roehl D. Three-dimensional extension of non-linear shell formulation based on the enhanced assumed strain concept. Int J Numer Methods Eng 1994;37(15):2551–68.
[39] Brank B, Korelc J, Ibrahimbegovic A. Nonlinear shell problem formulation accounting for through-the-thickness stretching and its finite element implementation. Comput Struct 2002;80(9–10):699–717.
[40] Kiendl J, Hsu M, Wu MC, Reali A. Isogeometric Kirchhoff-Love shell formulations for general hyperelastic materials. Comput Methods Appl Mech Eng 2015;291:280–303.
[41] Ambartsumian S. Nontraditional theories of shells and plates. Appl Mech Rev 2002;55(5):R35–44.
[42] Carrera E. Historical review of zig-zag theories for multilayered plates and shells. Appl Mech Rev 2003;56(3):287–308.
[43] Lekhnitskii S. Strength calculation of composite beams. Vestnik inzhen i tekhnikov 1935;9:137–48.
[44] Noor-E-Khuda S, Dhanasekar M, Thambiratnam D. Out-of-plane deformation and failure of masonry walls with various forms of reinforcement. Compos Struct 2016;140:262–77.
[45] Teng X, Zhang Y. Nonlinear finite element analyses of frp-strengthened reinforced concrete slabs using a new layered composite plate element. Compos Struct 2014;114(1):20–9.
[46] Valoroso N, Marmo F, Sessa S. Limit state analysis of reinforced shear walls. Eng Struct 2014;61:127–39.
[47] Valoroso N, Marmo F, Sessa S. A novel shell element for nonlinear pushover analysis of reinforced concrete shear walls. Bull Earthq Eng 2015;13(8):2367–88.
[48] Dvorkin EN, Bathe KJ. A continuum mechanics based four-node shell element for general non-linear analysis. Eng Comput 1984;1(1):77–88.
[49] Bathe K, Dvorkin EN. Four-node plate bending element based on Mindlin/Reissner plate theory and a mixed interpolation. Int J Numer Methods Eng 1985;21(2):367–83.
[50] Dvorkin EN, Pantuso D, Repetto EA. A formulation of the MITC4 shell element for finite strain elasto-plastic analysis. Comput Methods Appl Mech Eng 1995;125(1):17–40.
[51] Alfano G, Auricchio F, Rosati L, Sacco E. Mitc finite elements for laminated composite plates. Int J Numer Methods Eng 2001;50(3):707–38.
[52] S. Mazzoni, F. McKenna, M. H. Scott, G. L. Fenves, et al., Opensees command language manual, Pacific Earthquake Engineering Research (PEER) Center.
[53] Simo JC, Hughes TJ. Computational inelasticity, vol. 7. Springer Science & Business Media; 2006.
[54] Lubliner J. Plasticity theory. Courier Corporation; 2008.
[55] Karush W. Minima of functions of several variables with inequalities as side constraints. Ph.D. thesis, Master’s thesis. Dept. of Mathematics, Univ. of Chicago; 1939.
[56] Kuhn HW, Tucker AW. Nonlinear Programming. In: Proceedings of the Second Berkeley Symposium on Mathematical Statistics and Probability. Berkeley: University of California; 1951. p. 481–92.

[57] Suquet P. Thése de doctorat d'état. In: Plasticité et homogénéisation. Université Pierre et Marie Curie Paris; 1982.
[58] Germain P. Cours de mécanique des milieux continus, vol. 1. Masson; 1973.
[59] Nguyen N-T, Hui D, Lee J, Nguyen-Xuan H. An efficient computational approach for size-dependent analysis of functionally graded nanoplates. Comput Methods Appl Mech Eng 2015;297:191–218.
[60] Mindlin RD. Influence of rotary inertia and shear on flexural motions of isotropic elastic plates. J Appl Mech ASME 1951;18:31–8.
[61] Menegotto M, Pinto PE. Method of anaysis for cyclically loaded reinforced concrete plane frames including changes in geometry and non-elastic behavior of elements under combined normal force and bending. In: Proc., IABSE Symp. of resistance and ultimate deformability of structures acted on by WellDefined repeated loads, vol. 13. Libson, Portugal: International Association of Bridge and Structural Engineering; 1973. p. 15–22.
[62] European Union. EN 1992-1-1-Eurocode 2: design of concrete structures - Part 1-1: general rules and rules for buildings. 2004.
[63] Lubliner J, Oliver J, Oller S, Onate E. A plastic-damage model for concrete. Int J Solids Struct 1989;25(3):299–326.
[64] Serpieri R, Alfano G, Sacco E. A mixed-mode cohesive-zone model accounting for finite dilation and asperity degradation. Int J Solids Struct 2015;67:102–15.
[65] Carpentieri G, Modano M, Fabbrocino F, Feo L, Fraternali F. On the minimal mass reinforcement of masonry structures with arbitrary shapes. Meccanica 2016:1–16.
[66] Fraternali F, Carpentieri G, Modano M, Fabbrocino F, Skelton R. A tensegrity approach to the optimal reinforcement of masonry domes and vaults through fiber-reinforced composite materials. Compos Struct 2015;134:247–54.
[67] Fabbrocino F, Farina I, Berardi VP, Ferreira A, Fraternali F. On the thrust surface of unreinforced and frp-/frcm-reinforced masonry domes. Compos Part B Eng 2015;83:297–305.
[68] Marmo F, Rosati L. Reformulation and extension of the thrust network analysis. Comput Struct 2017;182:104–18.
[69] Menun C. An envelope for Mohr's circle in seismically excited three-dimensional structures. Earthq Eng Struct Dyn 2004;33(9):981–98.
[70] Sessa S, Marmo F, Rosati L. Effective use of seismic response envelopes for reinforced concrete structures. Earthq Eng Struct Dyn 2015;44(14):2401–23.
[71] Stewart JP, Fenves GL, Seed RB. Seismic soil-structure interaction in buildings. i: analytical methods. J Geotechnical Geoenvironmental Eng 1999;125(1):26–37.
[72] Gajan S, Raychowdhury P, Hutchinson TC, Kutter BL, Stewart JP. Application and validation of practical tools for nonlinear soil-foundation interaction analysis. Earthq Spectra 2010;26(1):111–29.
[73] Fatahi B, Tabatabaiefar SHR. Fully nonlinear versus equivalent linear computation method for seismic analysis of midrise buildings on soft soils. Int J Geomechanics 2014;14(4). 04014016–1 – 15.
[74] Marmo F, Sessa S, Rosati L. Analytical solution of the Cerruti problem under linearly distributed horizontal loads over polygonal domains. J Elast 2016;124(1):27–56.
[75] Marmo F, Rosati L. A general approach to the solution of boussinesq's problem for polynomial pressures acting over polygonal domains. J Elast 2016;122(1):75–112.